JGR Solid Earth

RESEARCH ARTICLE
10.1029/2020JB021536

Exact Analytical Solutions for Kinetic Equations Describing Thermochemical Remanence Acquisition for Single-Domain Grains: Implications for Absolute Paleointensity Determinations

V. P. Shcherbakov[1], F. Lhuillier[2], and N. K. Sycheva[1]

[1]Geophysical Observatory Borok, Yaroslavskaja Oblast, Russia, [2]Department of Earth and Environmental Sciences, Ludwig Maximilian University, Munich, Germany

Key Points:

- Analytical solutions for the kinetics of thermoremanent magnetization (TRM) and thermo-chemical remanent magnetization (TCRM) acquisition for single-domain grains are derived and used to construct Arai diagrams
- At fast cooling rate, TCRM acquired by Curie point increase yield reliable paleointensity estimates but not TCRM acquired by volume growth
- Slowly cooled TRMs yield reliable paleointensities provided geomagnetic secular variation is averaged and cooling-rate effect is corrected

Correspondence to:
F. Lhuillier,
lhuillier@geophysik.uni-muenchen.de

Citation:
Shcherbakov, V. P., Lhuillier, F., & Sycheva, N. K. (2021). Exact analytical solutions for kinetic equations describing thermochemical remanence acquisition for single-domain grains: Implications for absolute paleointensity determinations. *Journal of Geophysical Research: Solid Earth*, *126*, e2020JB021536. https://doi.org/10.1029/2020JB021536

Received 12 DEC 2020
Accepted 8 APR 2021

Abstract The magnetic record, preserved by igneous rocks in the form of thermoremanent magnetization (TRM) or thermo-chemical remanent magnetization (TCRM), is essential to reconstruct Earth's absolute paleointensity (API) but strongly depends on the kinetic conditions in which the remanence was acquired. In this paper, we present exact analytical solutions describing the time-dependent processes of acquisition and thermal demagnetization of various kinds of thermally activated remanences for non-interacting single-domain grains with uniaxial shape anisotropy. Our solutions, derived in less-restrictive conditions than previous studies, are also valid for TCRMs acquired either by growth of grain volume or by increase of the Curie point T_c. We first show that TCRMs by T_c increase and TRMs are of comparable intensity whereas TCRMs by volume growth are significantly less intense. We then model Arai-Nagata diagrams for assemblies of coercivity-variable grains and find that all Thellier-type protocols yield reliable API determinations for TRMs and TCRMs by T_c increase, with the peculiarity of the IZZI protocol to produce small zigzags in the Arai-Nagata diagram. In contrast, TCRMs by volume growth yield convex Arai-Nagata diagrams. The most conspicuous kinetic effect is the influence of cooling rate on API determinations due to a ~5% increase of the remanent magnetization for a 10-fold increase in cooling time. We show that the situation is problematic when the cooling time of natural samples coincides with the geomagnetic secular-variation time scales. Natural samples with cooling times sufficient to average out secular variation conversely yield reliable API determinations provided a cooling-rate correction is applied.

Plain Language Summary When a lava or a magma cools down, iron-rich minerals acquire magnetic properties while crossing their Curie point T_c and then fossilize the properties of the ambient magnetic field while passing through their blocking temperature. While rapidly cooled objects produce instantaneous records of Earth's magnetic field, called thermoremanences (TRMs), slowly cooled objects may be blurred by geomagnetic secular variation (SV) and additionally experience mineralogical transformations either due to the growth of grains or the increase of T_c, leading to more complex thermochemical remanent magnetizations (TCRMs). A big challenge of modern paleomagnetism is thus to identify the most appropriate remanences that yield robust paleointensity estimates. To address this issue, we derived analytical solutions that describe the acquisition and demagnetization processes of such remanences for assemblies of uniformly magnetized particles. We first show that TRMs and TCRMs by T_c increase yield equally robust paleointensities, whereas the magnetic signal is harder to deconvolve for TCRMs by grain growth. We then confirm that uncorrected contrasts in cooling rate between natural and laboratory conditions can strongly overestimate paleointensities. If the cooling rate exceeds the typical SV time scales, we demonstrate that average paleointensities, representative of geodynamo activity, can be robustly determined provided that a cooling-rate correction is applied.

1. Introduction

Absolute paleointensity (API) determinations are crucial for understanding the evolution of the ancient geomagnetic field (e.g., Tauxe & Yamazaki, 2015). In particular, spatio-temporal analysis of API can help to constrain the geodynamics of Earth's outer core, such as the possible relationship between geomagnetic reversal frequency and paleointensity (e.g., Ingham et al., 2014; Kulakov et al., 2019; Shcherbakov &

Sycheva, 2013) or the identification of key events of the geodynamo's history like, for example, the inner core's nucleation (e.g., Biggin et al., 2015; Smirnov et al., 2016; Tarduno et al., 2015). From a practical viewpoint, API determinations are mostly restricted to igneous rocks, the natural remanent magnetization (NRM) of which being in the ideal case a thermoremanent magnetization (TRM) acquired during the inital cooling of a lava/magma, in the presence of the ambient magnetic field, from above its Curie temperature T_c, or sometimes a thermochemical remanent magnetization (TCRM) involving the formation of ferromagnetic minerals below T_c. The TCRM formation in single-domain (SD) grains may occur either by grain-volume growth above the blocking volume V_b or by magneto-mineralogical transformations such as single- and hetero-phase oxidation processes leading to an increase of T_c above the current environmental temperature T_{env} (e.g., Dunlop & Özdemir, 1997; Stacey & Banerjee, 1974). Independent of magneto-mineralogical alteration, note that another possible mechanism for T_c increase is the reversible reordering of cations and/or vacancies in the crystal structure of intermediate titanomagnetite (e.g., Bowles et al., 2013; Bowles & Jackson, 2016; Jackson & Bowles, 2018).

An unsolved problem of paleomagnetism is to better understand TCRM properties, the ultimate goal being to find practical methods to unambiguously distinguish the various kinds of TCRMs and in particular those yielding unbiased API determinations (e.g., Draeger et al., 2006; Fabian, 2009; Shcherbakov, Gribov, et al., 2019; Smirnov & Tarduno, 2005). As rock samples usually cool down much faster in laboratory conditions than in natural conditions, another topical issue is the dependency of API determinations on cooling rate. From theoretical (e.g., Dodson & McClelland-Brown, 1980; Halgedahl et al., 1980; Walton, 1980) and experimental (e.g., Berndt et al., 2017; Berndt et al., 2021; Biggin et al., 2013; Ferk et al., 2014; Yu, 2011) results, it has been proposed that SD and pseudo-single domain (PSD) grains show larger TRMs after slow cooling than after fast cooling, whereas multidomain (MD) grains are slightly or not at all affected by variations in cooling rate. For SD grains, the dependency of TRM intensity on cooling rate is predicted to occur in a logarithmic manner, with a tenfold decrease in cooling rate leading to a ~5% increase in TRM intensity.

From a theoretical viewpoint, the acquisition of TRM or TCRM can be explained by Néel's (1949, 1955) theory. Before the blocking of TRM or TCRM occurs, an ensemble of identical grains with magnetic moment $\mathbf{m}$ and number density n is in a superparamagnetic (SP) state where its magnetization is

$$M = mn \tanh\left(\frac{\mathbf{m}\cdot\mathbf{B}}{k_B T}\right). \tag{1}$$

Here, k_B is Boltzmann's constant, T is the ambient temperature, and $\mathbf{B}$ is the external magnetic field. The kinetics of the magnetization is governed by the relaxation time

$$\tau = f_0^{-1} \exp\left(\frac{E_b}{k_B T}\right), \tag{2}$$

where $f_0^{-1} \approx 10^{-9}$ is the time for a single attempt to overcome the potential barrier E_b that prevents a reversal of the magnetic moment (e.g., Néel, 1955). During the magnetization process, the moment of the SD grain becomes frozen at the blocking temperature T_b at which the relaxation time τ equates a typical experimental time of usually 100 s (e.g., Bean & Livingston, 1959; Dunlop & Özdemir, 1997). Equations 1 and 2 thus lead to the blocking condition

$$E_b = 25 k_B T \tag{3}$$

and the TRM intensity

$$M_{TRM} = m\, n \tanh\left(\frac{\mathbf{m}(T_b)\cdot\mathbf{B}}{k_B T_b}\right). \tag{4}$$

Based on Néel's (1949, 1955) theory, protocols to retrieve API estimates commonly rely on variants of Thellier and Thellier's (1959) method, which replaces progressively a specimen's NRM with partial TRMs (pTRMs) imparted in a known laboratory field $\mathbf{B}_{lab}$ (e.g., Dunlop, 2011; Selkin & Tauxe, 2000; Valet, 2003,

for a review). In the original Thellier–Thellier protocol (Thellier & Thellier, 1959), the specimen is heated twice for each of multiple temperature steps, first in $+\mathbf{B}_{\text{lab}}$ and then in $-\mathbf{B}_{\text{lab}}$. In the Thellier–Coe variant (Coe, 1967), the specimen is first heated in a zero field, then imparted a pTRM in $+\mathbf{B}_{\text{lab}}$. In the Thellier–Aitken protocol (Aitken et al., 1988), the specimen is first applied a pTRM and then heated in a zero field. The Thellier-IZZI protocol (Tauxe & Staudigel, 2004; Yu et al., 2004) is a combination of the Thellier–Aitken and Thellier–Coe protocols, with a sequence of in-field and zero-field heating cycles (IZ) for a given temperature step, followed by a sequence of zero-field and in-field heating cycles (ZI) for the next temperature step. All these methods are thought to be virtually interchangeable in the case of ideal remanence carriers, although the Thellier-IZZI protocol is often claimed to be more efficient to detect the presence of MD remanence carriers (Tauxe & Staudigel, 2004).

In this study, we investigate the processes of acquisition and thermal demagnetization of TRM and TCRM assuming an ensemble of SD grains with uniaxial shape anisotropy such that

$$E_{\text{b}} = \mu_0 \, N_{\text{d}} M_{\text{S}}^2 \, V \, / \, 2. \tag{5}$$

Here, V is a grain's volume, M_{S} is its spontaneous magnetization, and $N_{\text{d}} = N_{\text{d}}^{\perp} - N_{\text{d}}^{\parallel}$ is the anisotropy parameter where $N_{\text{d}}^{\perp}$ (resp. $N_{\text{d}}^{\parallel}$) is the demagnetizing factor along the short axis (resp. long axis) of a grain. Some analytical solutions of the kinetic equations governing these processes have already been proposed by Dodson and McClelland-Brown (1980), Walton (1980), and Shcherbakov, McClelland, et al. (1993) with the intention of solving specific problems rather than offering a general description of the processes. These solutions were moreover derived in the framework of strong approximations—integration using saddle point methods in Walton (1980), linearization of Boltzmann's factor in Dodson and McClelland-Brown (1980)—and only considered the case of TRM acquisition whereas the understanding of the more complex case of TCRM acquisition is also of prime importance for the needs of rock magnetism. We note that numerical solutions of these kinetic equations are unfortunately hardly tractable due to the double exponential term that appears in the solutions, leading to extremely quick transitions from very low to very high values of the exponent in Equation 2. Based on analytical solutions, the purpose of this paper is thus to advance in the construction of a comprehensive theory describing the acquisition and thermal demagnetization of different kinds of thermally activated remanences for noninteracting SD grains starting from first principles, following the approach adopted by Egli and Lowrie (2002) in their theory of anhysteretic remanent magnetization. To this end, we present in Section 2 a new set of exact analytical solutions, valid not only for pure TRMs but also for different kinds of TCRMs, and derived under the sole mean-field approximation for the spontaneous magnetization. We detail in Section 3 the intrinsic characteristics of these solutions in terms of kinetic effects. We finally model in Section 4 Arai-Nagata diagrams (Nagata et al., 1963) for ensembles of SD grains with variable blocking temperatures, with an emphasis placed on the effects of varying cooling rate and averaging secular variation (SV) (Table 1).

2. Kinetic Equations and Their Solutions

Let x be the relative number of magnetic moments $\mathbf{m}$ of an ensemble of noninteracting SD grains, which are oriented parallel to the arbitrary positive direction along their light axis. Then, the function $x(t)$ obeys the known kinetic equation

$$\frac{\mathrm{d}x}{\mathrm{d}t} = -\frac{x}{\tau_1} + \frac{1-x}{\tau_2}, \tag{6}$$

where t is time and (τ_1, τ_2) are the Néel relaxation times defined by Equation 2 for flipping the moment from direction 1 to the opposite direction 2 (and vice versa) by overcoming the potential barrier

$$E_{\text{b1,2}} = \frac{\mu_0 \, N_{\text{d}} M_{\text{S}}^2 \, V}{2} - \mathbf{m}_{1,2} \cdot \mathbf{B}. \tag{7}$$

Table 1
List of Notations Used in This Paper

Notation	Meaning	Unit
μ_0	Vacuum permeability	H/m
k_B	Boltzmann's constant	J/K
n	Number density	m^{-3}
t	Time	s
τ	Néel relaxation time	s
f_0^{-1}	Atomic attempt time	s
λ	Heating/cooling time	s
λ_{lab}	Cooling time in laboratory conditions	s
λ_{NRM}	Cooling time of NRM acquisition	s
T	Temperature	K
T_r	Room temperature	K
T_{env}	Environmental temperature	K
T_0	Reaction temperature	K
T_c	Curie temperature	K
T_{c0}	Initial Curie temperature	K
T_{cf}	Final Curie temperature	K
T_b	Blocking temperature	K
T_{ub}	Unblocking temperature	K
$\mathcal{V}$	Sample volume	m^3
V	Current grain volume	m^3
V_f	Final grain volume	m^3
V_b	Blocking grain volume	m^3
m	Magnetic moment	$A \cdot m^2$
M	Magnetization	A/m
M_S	Spontaneous magnetization	A/m
M_{S0}	Spontaneous magnetization at $T = 0$ K	A/m
$N_d^{\perp}$	Demagnetizing factor along the short axis	Dimensionless
$N_d^{\parallel}$	Demagnetizing factor along the long axis	Dimensionless
N_d	Anisotropy parameter $\left[N_d^{\perp} - N_d^{\parallel}\right]$	Dimensionless
x	Relative number of moments	Dimensionless
y	Reduced magnetization	Dimensionless
β	Spontaneous magnetization $\left[M_S \,/\, M_{S0}\right]$	Dimensionless
g	Energy parameter $\left[(\mu_0 N_d M_{S0}^2 V) \,/\, (2k_B T_c)\right]$	Dimensionless
h	Field-intensity parameter $\left[(2B) \,/\, (3\mu_0 N_d M_{S0})\right]$	Dimensionless
q	Cooling-rate parameter $\left[\ln(2\lambda f_0)\right]$	Dimensionless
q_0	Rate in laboratory conditions $\left[\ln(2 f_0 \lambda_{lab})\right]$	Dimensionless
q_1	Cooling-rate ratio $\left[\log_{10}(\lambda_{NRM} \,/\, \lambda_{lab})\right]$	Dimensionless

Table 1
Continued

Notation	Meaning	Unit
θ	Reduced temperature $\left[T\ /\ T_c\right]$	Dimensionless
θ_c	Reduced Curie temperature $\left[T_c\ /\ T_{cf}\right]$	Dimensionless
θ_b	Reduced blocking temperature $\left[T_b\ /\ T_c\right]$	Dimensionless
θ_{b0}	Laboratory blocking temperature $\left[(T_b\ /\ T_c)_{q=25.3}\right]$	Dimensionless
v	Reduced grain volume $\left[V\ /\ V_f\right]$	Dimensionless

Introducing the reduced magnetization $y = 2x - 1$ as the magnetization normalized by $m\ n$ and assuming small external field such that $m\ B/k_B\ T \ll 1$, we arrive at

$$\frac{dy}{dt} = -2f_0 \exp\left(-\frac{\mu_0\ N_d M_S^2\ V}{2k_B T}\right)\left(y - \frac{\mathbf{m}\cdot\mathbf{B}}{k_B T}\right). \tag{8}$$

Here, the term $(\mathbf{m}\cdot\mathbf{B})/(k_B\ T)$ approximates the SP susceptibility for small fields. At high temperatures, that is, at the condition $\log(2f_0) \gg (\mu_0\ N_d M_S^2\ V)\ /\ (2k_B T)$, the factor $2f_0 \exp\left[-(\mu_0\ N_d M_S^2\ V)\ /\ (2k_B T)\right]$ in the right-hand side of Equation 8 approaches $2f_0$ as T approaches T_c, thus securing the SP behavior of the grains with the trivial solution $y = (\mathbf{m}\cdot\mathbf{B})/(k_B\ T)$. On the contrary, at low temperatures, that is, when $\log(2f_0) \ll (\mu_0\ N_d M_S^2\ V)\ /\ (2k_B T)$, the same factor becomes negligible leading to the solution $y =$ constant and the blocking of the magnetic moments. Hence, all magnetization and demagnetization processes occur in a temperature range between these two end-member cases.

2.1. TRM Acquisition and Demagnetization

Let us first consider the case of TRM acquisition which by definition takes place at constant grain volume V and constant Curie temperature T_c by cooling down a sample from T_c to the room temperature T_r. Let $M_S(T)$ be the spontaneous magnetization. The total magnetization of the ensemble of grains, normalized by $M_{S0} = M_S(T = 0\ \mathrm{K})$, can be written as $\beta(T)\cdot y(T)$, where $\beta(T) = M_S(T)/M_{S0}$ is the normalized spontaneous magnetization. Introducing the dimensionless temperature $\theta = T/T_c$ and assuming the linear dependency $\theta = \theta_0 \pm t/\lambda$, where the parameter λ is the time of heating or cooling, Equation 8 can be transformed into

$$\pm\frac{dy}{d\theta} = -A(\theta)y + D(\theta), \tag{9}$$

with the coefficients

$$A(\theta) = \exp\left(q + g - \frac{g}{\theta}\right), \tag{10}$$

$$D(\theta) = A(\theta) g\ h\frac{\sqrt{1-\theta}}{\theta}, \tag{11}$$

and the parameters

$$g = \frac{\mu_0\ N_d M_{S0}^2\ V}{2k_B\ T_c}, \tag{12}$$

$$q = \ln(2\lambda f_0), \tag{13}$$

$$h = 2B / (3\mu_0 N_d M_{S0}). \tag{14}$$

The quantities g, q, and h are respectively termed energy, cooling-rate, and field-intensity parameters in the rest of the paper. The parameter g actually represents the ratio of the self-demagnetizing energy (at $T = 0$ K) to the thermal energy (at $T = T_c$). Note that the linear dependency $\theta(t) = \theta_0 \pm t/\lambda$ can be justified by the fact that the temperature interval over which the TRM is acquired is narrow in comparison to the complete cooling time of the rock. We show in Appendix A that Equation 8 can also be easily integrated for the more realistic exponential dependency $\theta(t) = \theta_0 \exp(-t/\lambda)$. However, as the two dependencies produce insignificant differences on the reduced magnetization, we thus considered the simplest case of a linear dependency in this paper.

In the derivation of Equations 9–11, we employed the mean-field approximation $\beta(\theta) = (1 - \theta)^{1/2}$ for the temperature dependence of the spontaneous magnetization and note that the factor 3 in Equation 14 stems from averaging over $\mathbf{m} \cdot \mathbf{B}$. In laboratory conditions, the heating or cooling of a sample usually takes 10–20 min; therefore, we considered the value $\lambda_{lab} = 1000$ s. Taking $2f_0 = 10^8$ s^{-1} (for the choice of this value, see Shcherbakov & Fabian, 2005) led us to choose the value $q = 25.3$ for the cooling-rate parameter except in Sections 3.3 and 4.5 where the influence of cooling rate was investigated (e.g., Brown, 1962; Néel, 1955). We note that this value is very close to the value $q = 25$ recommended by Dunlop and Özdemir (1997).

In the case of pTRM or full TRM demagnetization, that is, when a sample is heated from θ to θ_i, a positive sign has to be chosen in the left-hand side of Equation 9, leading to the general solution

$$y(\theta) = C_1 e^{-f(\theta)} + \int_\theta^{\theta_i} D(x) e^{-f(\theta)+f(x)} \mathrm{d}x, \qquad C_1 e^{-f(\theta_1)} = y_1. \tag{15}$$

where

$$f(\theta) = \int A(x)\,\mathrm{d}x = \theta e^{(q+g-g/\theta)} - g\Gamma(0, g/\theta) e^{(q+g)} \tag{16}$$

with C_1 being an integration constant and $\Gamma(0,x) = \int_x^\infty e^{-x}/x \mathrm{d}x$ the incomplete gamma function.

In the case of pTRM acquisition, that is, when a sample is cooled from θ to θ_i, the signs of $f(\theta)$ and $D(\theta)$ have to be reversed, as well as the bounds of integration of Equation 9. We thus arrive at

$$y(\theta) = C_1 e^{f(\theta)} + \int_\theta^{\theta_i} D(x) e^{f(\theta)-f(x)} \mathrm{d}x, \qquad C_1 e^{f(\theta_1)} = y_1. \tag{17}$$

As illustrated in Figure 1a, studying the behavior of the reduced magnetization $y(\theta)$ rather than the product $\beta(\theta) \cdot y(\theta)$ better reveals the blocking effects. For the sake of simplicity, we used a constant parameter N_d and the same external field intensity B for both TRM and pTRM acquisition, noting that these simplifications can be easily abandoned if needed. In particular, to take the influence of the distribution of N_d into account, it would be possible to introduce distribution functions $f_1(N_d)$ and then obtain the solutions by an additional integration over $f_1(N_d)$. Finally, we note that $y(\theta)$ linearly depends on h as long as we study TRM acquisition under the action of thermal fluctuations and a small field B. For the sake of simplicity, we thus set h to one unless otherwise noted.

2.2. Concept of Blocking Temperature

In violation of Thellier's law of independence, Equation 15 predicts a nonzero reduced magnetization $y(\theta)$ until T_c is reached. It implies that the blocking/unblocking processes are not instantaneous as illustrated in Figure 2a, which compares the thermomagnetic curves $y(\theta)$ during the TRM acquisition and during the TRM demagnetization for an ensemble of SD grains with energy parameter $g = 150$.

The blocking process extends over some temperature interval, commencing when $y(\tau)$ deflects from the reference curve $y(\theta) = \sqrt{1-\theta}/\theta$ for an ensemble of SP grains at equilibrium and terminating when $y(\theta)$ reaches a plateau. Although this phenomenon has been known since Néel (1949, 1955), it is usually ignored

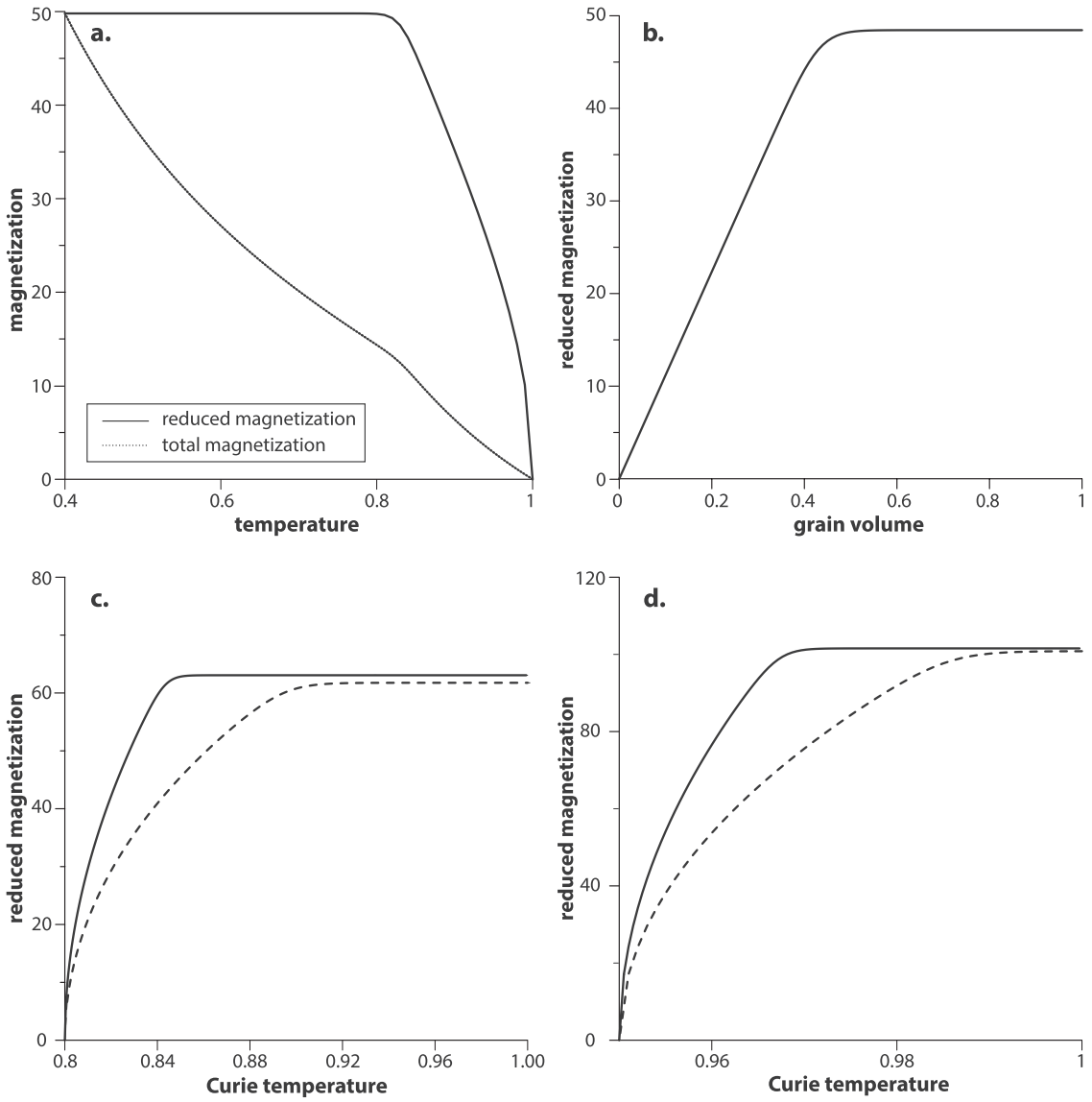

Figure 1. Examples of remanence acquisition from kinetic equations of Section 2. (a) TRM acquisition showing the reduced magnetization $y(\theta)$ (solid line) and the total magnetization $\beta(\theta) \cdot y(\theta)$ (dotted line) for an ensemble of identical SD grains with energy parameter $g = 100$. The function $y(\theta)$ is given in h units (see Section 2.1). (b) TCRM acquired by grain-volume increase showing the function $y(v)$ for $g = 200$ and the reaction temperature $\theta_0 = 0.8$. (c) TCRM acquired by T_c increase showing the function $y(\theta_c)$ for $g = 150$ and $\theta_0 = 0.8$. (d) TCRM acquired by T_c increase showing the function $y(\theta_c)$ for $g = 500$ and $\theta_0 = 0.95$. For panels (c) and (d), the dashed lines correspond to TRCM acquisition by increasing T_c at constant environmental temperature T_{env} (Section 2.3) while the solid lines correspond to TCRM acquisition by simultaneously increasing T_c and decreasing T_{env} (Section 2.4).

because the transition from a SP to a frozen state occurs over a narrow temperature range that is in general proportional to $2/g$ as evidenced by Equation 10. From a graphical point of view, the average blocking temperature θ_b can be defined as the point of maximum curvature of the TRM acquisition curve (represented by a circle in Figure 2). However, such definition do not allow one to derive a suitable analytical expression for T_b.

Because of the similarity of the critical temperature intervals over which the blocking and unblocking processes take place, we approximate in this paper θ_b by the average unblocking temperature θ_{ub}, following the common practice for SD grains. From a mathematical point of view, θ_{ub} can be defined as the point of steepest descent on the TRM demagnetization curve. Then, equating the second order derivative of $y(\tau)$ to zero leads to the relationship

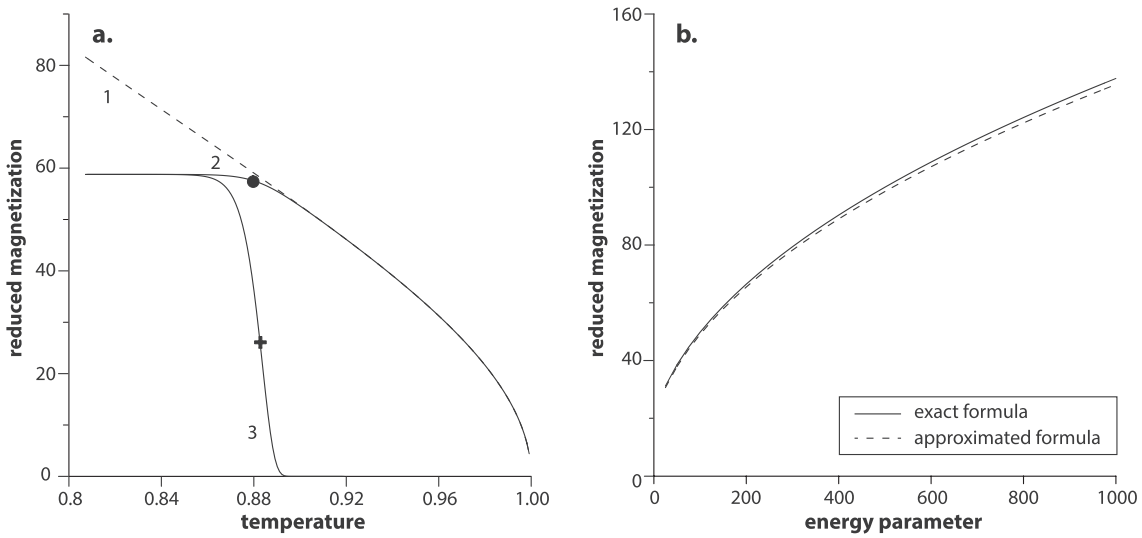

Figure 2. Concept of blocking temperature. (a) Example of TRM acquisition and thermal demagnetization for energy parameter $g = 150$. Curve 1 (dashed line) shows the reference curve $y(\theta) = \sqrt{1-\theta}\ /\ \theta$ for an ensemble of SP grains at equilibrium. Curve 2 shows the reduced magnetization $y(\theta)$ during the TRM acquisition. The disk represents the point of maximum curvature. Curve 3 shows $y(\theta)$ during the thermal demagnetization of the acquired TRM. The cross represents the point of steepest descent, the abscissa of which approximates the blocking temperature θ_b (see Section 2.2). (b) Approximated TRM intensity (dashed line, from Equations 19 and 21) compared to exact TRM intensity (solid line, from Equation 17) at room temperature.

$$\exp\left\{g+q-\frac{g}{\theta}-e^{q}\left[\theta e^{g-g/\theta}-g e^{g}\Gamma\left(0,g\ /\ \theta\right)\right]\right\}\left\{\frac{g}{\theta^{2}}-e^{g+q-g/\theta}\right\}=0 \tag{18}$$

that can be simplified into

$$g\frac{1-\theta}{\theta}=\ln\left(\frac{2f_0\,\theta^2}{g}\right). \tag{19}$$

Using the relationships 12 and 13 and the definition $\theta = T/T_c$, we arrive, in terms of physical variables, at the relationship

$$\frac{E_b}{k_B T}=\ln\left[\frac{2f_0}{\frac{\mathrm{d}}{\mathrm{d}t}\left(\frac{E_b}{k_B T}\right)}\right] \tag{20}$$

accounting for the fact that, in our notations, $E_b/k_B\,T = g/\theta$ and $\mathrm{d}[E_b/(k_B\,T)]/\mathrm{d}t = \lambda/\theta^2$. Equation 20 only insignificantly differs, by a term equal to Euler–Mascheroni constant $\gamma \approx 0.577$, from the relationship obtained by York (1978), Dodson and McClelland-Brown (1980), and Walton (1980). Remind that Dodson and McClelland-Brown (1980) had defined T_b as the intersection of the asymptotic branch of the TRM acquisition curve with the reference curve $y(\theta) = \sqrt{1-\theta}\ /\ \theta$ for an ensemble of SP grains at equilibrium.

With regard to the applications, the most common usage of the blocking temperature concept is the calculation of the TRM intensity by substituting its value into the formula for the SP magnetization, yielding in our case

$$y(\theta)=g\frac{(1-\theta)^{1/2}}{\theta}\quad \text{at } \theta=\theta_b. \tag{21}$$

As illustrated in Figure 2b, this approximate formula to estimate TRM intensity closely coincides with the exact formula.

2.3. TCRM Acquisition by Grain-Volume Increase

Let us second consider the case when TCRM is acquired by increasing linearly with time the current grain volume V from zero to its final value V_f at a fixed dimensionless temperature θ_0. For the sake of convenience, we introduce the dimensionless volume $v = V/V_f$ that linearly increases from 0 to 1, so that $v = t/\lambda$. Equation 8 can be transformed into

$$\frac{dy}{dv} = -A(v)\, y + D(v) \tag{22}$$

with the coefficients

$$A(v) = \exp\left[q - \frac{g(1-\theta_0)}{\theta_0} v\right], \tag{23}$$

$$D(v) = A(v) g\, h\, v \frac{\sqrt{1-\theta_0}}{\theta_0}. \tag{24}$$

The general solution of Equation 22 is given as previously by Equation 15 with

$$f(v) = \int A(v)\, dv = -\frac{\exp\left[q - \frac{g(1-\theta_0)}{\theta_0} v\right]\theta_0}{g(1-\theta_0)}. \tag{25}$$

For the initial condition $v = 0$, the solution of Equation 22 thus becomes

$$y(v) = \frac{g\, v(1-\theta_0) - \theta_0 \exp\left\{\frac{\theta_0 \exp\left[q - gv(1-\theta_0)/\theta_0\right]}{g(1-\theta_0)}\right\}\left\{\Gamma\left[0, \frac{\theta_0 \exp\left[q - gv(1-\theta_0)/\theta_0\right]}{g(1-\theta_0)}\right] - \Gamma\left[0, \frac{\exp(q)\theta_0}{g(1-\theta_0)}\right]\right\}}{\theta_0 (1-\theta_0)^{1/2}}. \tag{26}$$

where $\Gamma(0, x)$ is as previously the incomplete gamma function. Figure 1b illustrates an example of such TCRM acquisition by grain-volume increase.

2.4. TCRM Acquisition by Curie Temperature Increase

Let us third consider the case when TCRM is acquired by increasing T_c from a fixed temperature T_{c0} to its final value T_{cf}. Introducing the dimensionless temperature $\theta_c(t) = T_c(t)/T_{cf}$ and assuming the linear relationship $\theta(t) = \theta_0 + t/\lambda$ with $\theta_0 = T_{c0}/T_{cf}$, we obtain, for the coefficients of Equation 22, the following expressions

$$A(\tau_c) = \exp\left(q - \frac{g}{\theta_0} + \frac{g}{\theta_c}\right), \tag{27}$$

$$D(\tau_c) = A(\theta_c)\, g\, h \frac{\sqrt{1 - \theta_0/\theta_c}}{\theta_0}. \tag{28}$$

From these equations, we get the function

$$f(\theta_c) = \int A(\theta_c)\,d\theta_c = \exp(q - g/\theta_0)\left[\theta_c \exp(g/\theta_c) + g\Gamma(0, -g/\theta_c)\right], \quad (29)$$

and the solution of Equation 15 for the initial condition $y(\theta_0) = 0$ can be expressed as

$$y(\theta_c) = \int_{\theta_0}^{\theta_c} D(x) \exp\left[-f(\theta_c) + f(x)\right] dx. \quad (30)$$

Figures 1c and 1d (dashed curves) illustrate two examples of TCRM acquisition by T_c increase.

2.5. TCRM Acquisition by T_c Increase and T_{env} Decrease

In the general case of TCRM acquisition, both environmental temperature T_{env} and Curie temperature T_c change with time. This leads to transform Equation 27 into

$$A(t) = \exp\left[\log(2f_0) - g\frac{\theta_c(t) - \theta(t)}{\theta_c(t)\cdot\theta(t)}\right]. \quad (31)$$

If $\theta(t)$ changes much more rapidly than $\theta_c(t)$, we return to the case of pTRM (or TRM if θ_0 is very close to one) acquisition described in Section 2.1. Conversely, if $\theta_c(t)$ changes much more rapidly than $\theta(t)$, it approximates the mechanism of TCRM acquisition described in Section 2.3, when θ_c increases while T_{env} is almost constant.

Unfortunately, the coefficient $A(t)$ given by Equation 31 cannot be integrated in a close form in the general case. However, we can consider a particular case when the difference $z(t) = \theta_c(t) - \theta(t)$ linearly increases with time while the product $\theta_c(t)\cdot\theta(t)$ is constant, namely,

$$z(t) = \alpha t, \quad (32)$$

$$\theta_c(t)\cdot\theta(t) = \theta_0^2. \quad (33)$$

In this case, the coefficients of Equation 22 are

$$A(z) = \exp\left[q - g\frac{z}{\theta_0^2}\right], \quad (34)$$

$$D(z) = A(z)\, g\, h\frac{\sqrt{z/\theta_{c1}}}{\theta}. \quad (35)$$

Here, θ_1 and θ_{c1} are, respectively, the positive roots of the quadratic equations

$$\theta - \frac{\theta_0^2}{\theta} + z = 0, \quad (36)$$

$$\theta_c - \frac{\theta_0^2}{\theta_c} + z = 0. \quad (37)$$

As $\theta_c(t) \le 1$, the value of z cannot exceed 1. For the initial condition $y = 0$ at $z = 0$, the reduced magnetization becomes

$$y(z) = \int_0^z D(x) \exp\left[f(x) - f(z)\right] dx, \quad 0 \le z \le 1 - \theta_0^2 \quad (38)$$

with

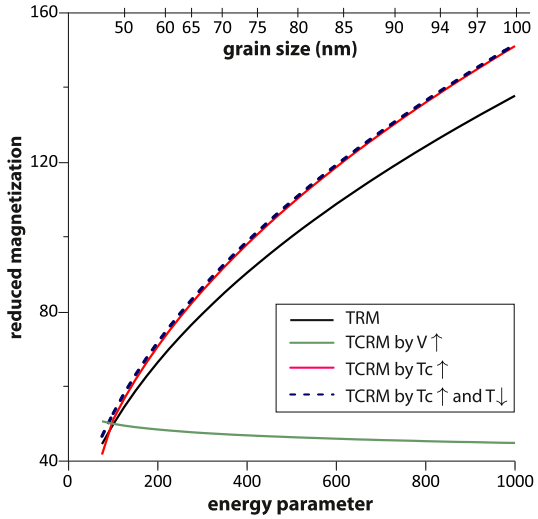

Figure 3. Reduced magnetization $y(\theta_r)$ at room temperature as a function of energy parameter g for various types of thermally activated remanences. The green line shows the intensity of the TCRM acquired by grain-volume growth calculated from Equation 26 at $v = 1$. The black solid line shows the intensity of the TRM calculated from Equation 17 at $\theta = \theta_r$ and $C_1 = 0$. The red line shows the intensity of the TCRM acquired by T_c increase calculated from Equation 30 at $\theta_c = 1$. The black dashed line shows the intensity of the TCRM acquired by both T_c increase and T_{env} decrease calculated from Equation 38 at $z = 1 - \theta_0^2$. All calculations were made at the reaction temperature $\theta_0 = 0.8$. The upper x-axis indicates the equivalent grain size for magnetite when $M_{S0} = 485{,}000$ A/m and $N_d = 1/(4\pi)$.

$$f(z) = \int A(z)\,dz = -\frac{\theta_0^2 \exp\left(q - \frac{g\,z}{\theta_0^2}\right)}{g}. \quad (39)$$

Examples of TCRM acquisition for this more general case are given in Figures 1c and 1d (solid lines), to be compared with TRM acquisition by T_c increase at constant environmental temperature (dashed lines). It appears that the blocking occurs at lower T_c due to the decrease of T_{env}, leading to a slightly enhanced intensity.

3. Kinetic Consequences of These Solutions

3.1. Comparison Between TRM and TCRM Intensities

In this section, we first compare TRM and TCRM intensities as a function of energy parameter g. Figure 3 reveals a distinctive behavior for TCRM acquired by volume growth and TCRM acquired by T_c increase. On the one hand, TCRM acquired by increasing T_c at a constant environmental temperature T_{env} and TCRM acquired by both increasing T_c and decreasing T_{env} are practically indistinguishable. They are moreover indistinguishable from a pure TRM at a low g values while an intensity excess of ca. 5% is observed at high g values. On the other hand, TCRM acquired by grain-volume growth is significantly weaker than a pure TRM. These observations confirm experimental results (e.g., Draeger et al., 2006; Shcherbakov, Gribov, et al., 2019) according to which TCRM acquired by T_c increase would produce almost unbiased API determinations whereas TCRM acquired by grain-volume growth would not be suitable for API determinations.

Note that the curves in Figure 3 were drawn starting from $g = 80$, which is equivalent to a blocking temperature $\theta_b = 0.8$ according to Equation 19, to insure that a remanence is acquired (i.e., θ_b always exceeds the reaction temperature $\tau_0 = 0.8$). The upper x-axis indicates the equivalent grain size for magnetite when $M_{S0} = 485{,}000$ A/m and $N_d = 1/(4\pi)$. This latter value corresponds to an oblate spheroid with a ratio of 0.816 of the length of the short axis to the length of the long axis, namely a rather moderate deflection from shape isotropy.

3.2. Comparison Between TRM Lost and pTRM Gained

We now more specifically focus on pure TRMs and compare the amplitude of the TRM loss (defined as the difference between the total TRM and its rest at room temperature T_r) and the pTRM gain while considering various combinations of heating-cooling cycles that mimic Thellier-style experiments at a given temperature step.

For any temperature step of the most commonly employed Thellier-Coe protocol (Coe, 1967), the sample is submitted to a sequence of a zero-field heating-cooling cycle followed by an in-field heating–cooling cycle. We assumed here that the direction of the external field is identical for the TRM and pTRM acquisitions. Figure 4a illustrates this case for heating-cooling cycles up to $\theta_i = 0.83$ and reveals that the TRM loss (≈ 35.5) considerably exceeds the pTRM gain (≈ 25). In other words, there is no total restoration of the TRM despite the same external fields were applied for the TRM and pTRM acquisitions. It implies in this case an underestimation of the ancient field. However, more rigorous modeling of API experiments for an ensemble of coercivity-variable SD grains (Section 3.3) will show that these kinetics effects are partly canceled due to the presence of grains with blocking temperatures θ_b outside the interval around θ_i. If the reverse sequence of heating-cooling cycles is applied following the example of the Thellier-Aitken protocol (Aitken et al., 1988),

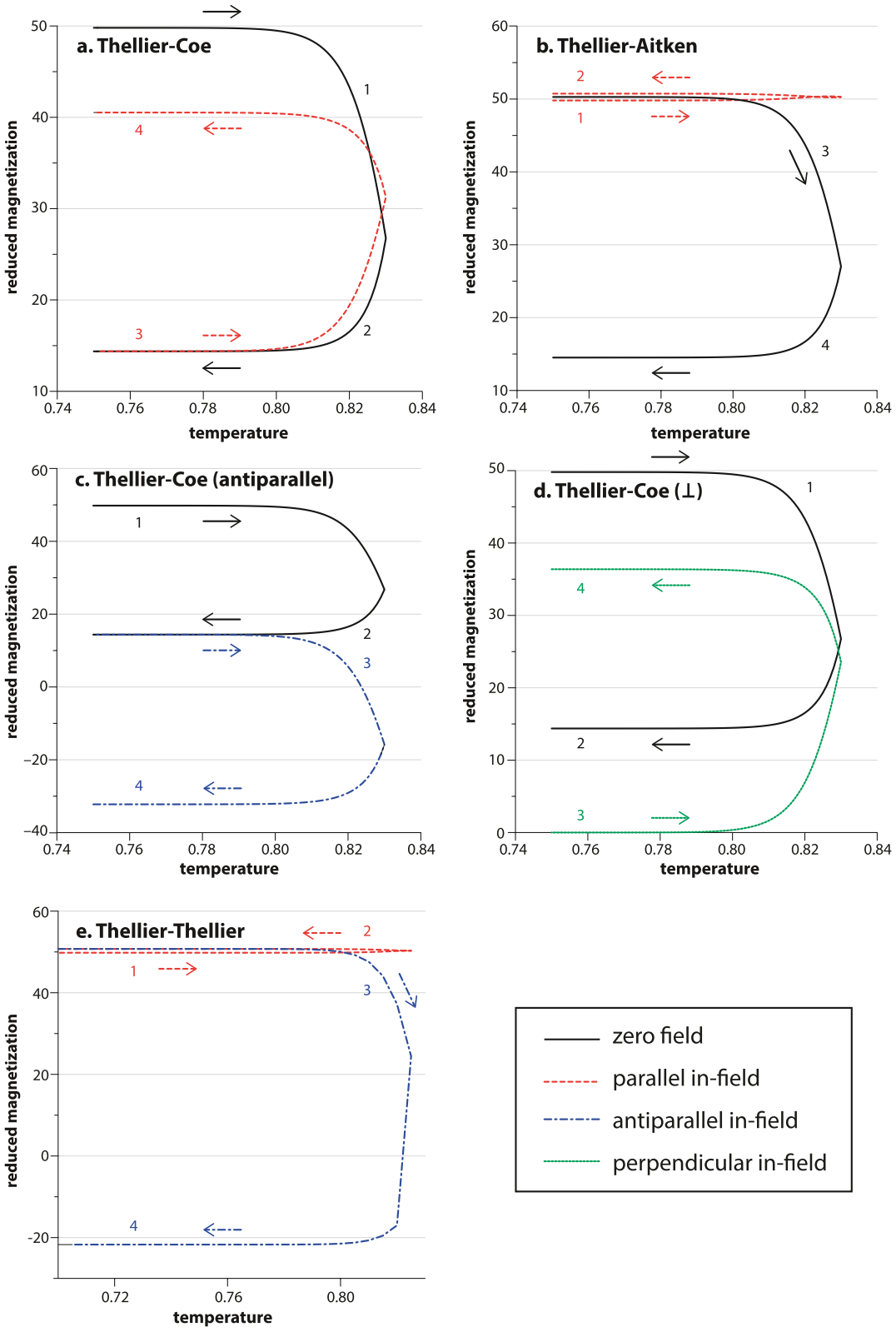
a. Thellier-Coe
b. Thellier-Aitken
c. Thellier-Coe (antiparallel)
d. Thellier-Coe (⊥)
e. Thellier-Thellier
reduced magnetization
temperature
zero field
parallel in-field
antiparallel in-field
perpendicular in-field

Figure 4b shows that the pTRM gain closely equates the TRM loss. Seen from that viewpoint, the Thellier-Aitken protocol would thus be more preferable than the Thellier-Coe protocol for API experiments.

More generally, the external field $\mathbf{B}_{\rm lab}$ can be applied in different directions for the TRM and pTRM acquisitions, with known consequences for API determinations. A detailed analysis of this problem that requires consideration of the geometry of the mutual disposition of TRM acquisition field, laboratory field and easy axis directions is above the scope of the study. However, for the purpose of this paper, we consider the two end-member cases when the TRM and pTRM are applied in antiparallel or orthogonal directions. Figure 4c presents the case of the Thellier-Coe procedure when the pTRM is applied in an antiparallel direction ($h = -1$) and reveals that the pTRM gain (≈ 46.5) leads to a 30% overestimation with respect to the TRM loss (≈ 35.5), compared to a 30% underestimation for $h = +1$. Figure 4d presents the case of the Thellier–Coe procedure when the laboratory field is applied orthogonal to the TRM direction (e.g., Kono, 1974). To calculate the corresponding kinetic curves, we used the fact that the creation and thermal demagnetization of TRM (first heating-cooling cycle) and pTRM (second heating-cooling cycle) are independent processes due to the orthogonality of their magnetizations. We observe that this protocol yields a pTRM gain (≈ 36.4) very close to the TRM loss (≈ 35.5).

We finally consider in Figure 4e the case of the original Thellier-Thellier protocol (Thellier & Thellier, 1959) that consists of a first heating-cooling cycle in the direction $+\mathbf{B}_{\rm lab}$ followed by a second heating-cooling cycle in the direction $-\mathbf{B}_{\rm lab}$ for each temperature step. Starting from a given primary TRM (TRM0 = 49.8 in our case), the first heating-cooling cycle yields the reduced magnetization $y_1 = \text{TRM} + \text{pTRM} = 50.7$ while the second heating-cooling cycle yields the reduced magnetization $y_2 = \text{TRM} - \text{pTRM} = -21.7$. The TRM loss ($= \text{TRM0} - (y_1 + y_2)/2 = 35.3$) is thus very close to the pTRM gain ($= (y_1 - y_2)/2 = 36.2$) like in the case of Thellier-Aitken and "perpendicular fields" protocols.

3.3. Dependence of Cooling Rate on TRM Intensity

We finally focus on the dependence of cooling rate on TRM intensity. To compare the remanence acquired in natural conditions (called hereinafter NRM) to the remanence acquired in laboratory conditions in the course of Thellier-type experiments (called hereinafter TRM), we express the cooling-rate parameter q defined by Equation 13 such that

$$\begin{aligned} q &= q_0 + \ln(10)\, q_1 \\ q_0 &= \ln(2 f_0 \lambda_{\rm lab}) \\ q_1 &= \log_{10}(\lambda_{\rm NRM} \,/\, \lambda_{\rm lab}) \end{aligned} \tag{40}$$

where $\lambda_{\rm lab} = 1000$ s is the typical cooling time of laboratory experiments and $\lambda_{\rm NRM}$ is the cooling time of NRM acquisition. The dependency of the blocking temperature $\theta_{\rm b}$ on the parameters g and q_1, calculated from Equation 19, is shown in Figure 5a. The NRM/TRM ratio can first be expressed as a function of g and q_1 using Equation 17, then as a function of q_1 and $\theta_{\rm b0}$ using Equation 19, where $\theta_{\rm b0}$ is the blocking temperature in laboratory conditions, that is, for $q = 25.3$.

As illustrated in Figure 5b, the cooling-rate effect only slightly depends on $\theta_{\rm b0}$ provided that $\theta_{\rm b0} > 0.5$. In agreement with Dodson and McClelland-Brown (1980), Walton (1980), and Halgedahl et al. (1980), the NRM/TRM ratio is overestimated by approximately 5% for a tenfold increase of the cooling time. In the particular case when $\theta_{\rm b0} \le 0.5$, the NRM/TRM ratio rapidly reaches a plateau as the corresponding blocking temperatures $\theta_{\rm b0}(g, q_1)$ fall below the environmental temperature $\theta_{\rm env} \approx 0.35$, which is considered to be the lowest temperature available for a sample during cooling both in natural and laboratory conditions. Consequently, the intensity of the reduced magnetization becomes frozen at $\theta_{\rm env}$. Formally, this condition was satisfied by equating the lower bound in the integral of Equation 17 to $\theta_{\rm env}$.

Figure 4. Continuous thermomagnetic curves of the reduced magnetization $y(\theta)$ to an intermediate temperature $\theta_i = 0.83$ for an ensemble of identical SD grains with parameters $g = 100$ and $q = 25$. (a) Zero-field heating–cooling cycle (curves 1–2) followed by an in-field heating–cooling cycle (curves 3–4), following the example of the Thellier–Coe protocol. (b) In-field heating–cooling cycle (curves 1–2) followed by a zero-field heating–cooling (curves 3–4), following the example of the Thellier–Aitken protocol. (c) Same as panel (a) for a laboratory field antiparallel to the TRM direction. (d) Same as panel (a) for a laboratory field perpendicular to the TRM direction. (e) Example of the Classical Thellier method with opposite fields applied for the first and second cycles.

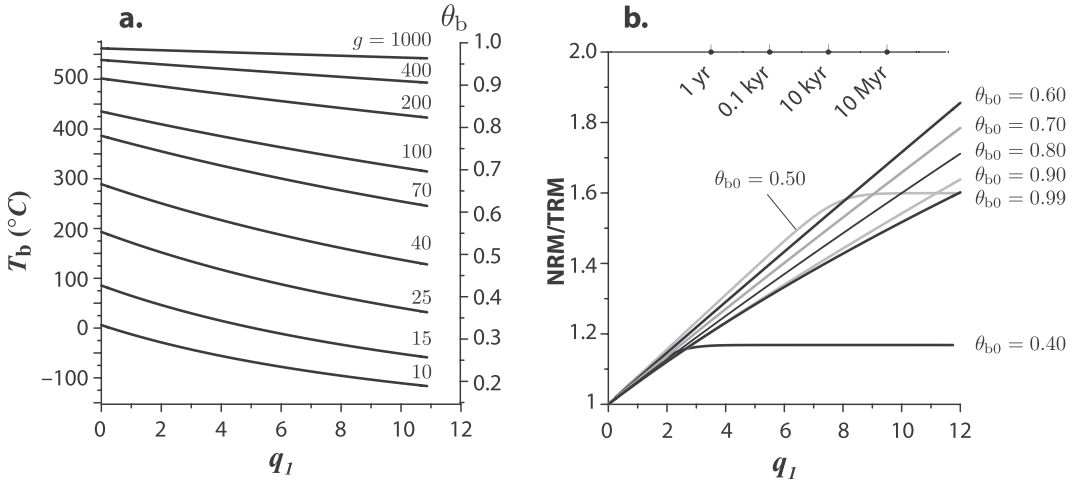

Figure 5. Dependence of cooling rate on TRM intensity. (a) Blocking temperature T_b as a function of $q_1 = \log_{10}(\lambda_{NRM}/\lambda_{lab})$ for different values of energy parameter (g) (b) NRM/TRM ratio as functions of q_1 and blocking temperature θ_{b0} calculated at $q_1 = 0$.

4. Modeling Arai-Nagata Diagrams

4.1. Method

In this section, we simulate more complete Thellier-style experiments. The TRM acquired by an ensemble of noninteracting SD grains is

$$M(\theta) = \frac{M_S(\theta)}{\mathcal{V}} \int V\, n(V)\, y[V,\theta]\, dV \tag{41}$$

where $y(V, \theta)$ is the reduced magnetization defined by Equation 15 or 17 that here additionally depends on grain volume V. The density $n(V)$ gives the number of grains with volume V and satisfies the normalization condition

$$N_0 = \int n(V)\, dV \tag{42}$$

where N_0 is the total number of grains inside the sample's volume $\mathcal{V}$. Remind that the energy parameter g and grain volume V are linearly linked by Equation 12. It is thus more common to calculate pTRMs using the blocking temperature spectrum $n(\theta_{b0})$. Using Equation 19 that links g to the blocking temperature θ_{b0} in laboratory conditions, we can transform Equation 41 into

$$\begin{aligned} M(\theta) &= \frac{M_S(\theta)}{\mathcal{V}} \int V(\theta_{b0})\, n[V(\theta_{b0})]\, y[g(\theta_{b0}),\theta] \frac{dV}{d\theta_{b0}} d\theta_{b0}, \\ &= M_S(\theta) \int C(\theta_{b0})\, y[g(\theta_{b0}),\theta]\, d\theta_{b0}, \end{aligned} \tag{43}$$

where we introduced the relative volume concentration

$$C(\theta_{b0}) = \frac{V(\theta_{b0})\, n[V(\theta_{b0})]}{\mathcal{V}} \frac{dV}{d\theta_{b0}} \tag{44}$$

and integrated over the spectrum of θ_{b0}.

For the sake of simplicity, we set $C(\theta_{b0})$ to a constant for $1 > \theta_{b0} > \theta_{low}$ and $C(\theta_{b0})$ to zero for $\theta_{b0} < \theta_{low}$, where θ_{low} is the low boundary of the spectrum of θ_{b0}. Obviously, this restriction can be easily removed if needed by specifying a particular spectrum of $C(\theta_{b0})$. In these conditions, the magnetization of the ensemble becomes

$$M(\theta) = M_{\rm sat}(\theta) \int_{\theta_{\rm low}}^{1} y(\theta_{\rm b0}, \theta)\, {\rm d}\theta_{\rm b0}, \tag{45}$$

where $M_{\rm sat}$ is the saturation magnetization of the sample. For the modeling of Arai-Nagata diagrams (Nagata et al., 1963), we can thus find the relative pTRM and TCRM values, at the normalized room temperature $\theta_{\rm r}$, by simple summation

$$M(\theta_{\rm r}) = M_{\rm sat}(\theta_{\rm r})\, \delta\theta_{\rm b0} \sum_{\theta_{\rm low}}^{\tau_i} y(\theta_{\rm b0}, \theta_{\rm r}) \tag{46}$$

over $\theta_{\rm b0}(i)$ with a small step $\delta\theta_{\rm b0}$ to determine the NRM loss (respectively, the pTRM gained) using the algorithm developed in Section 2.1.

4.2. Results for TRM and TCRM

Figure 6a shows the Arai-Nagata diagram for an ensemble of noninteracting SD particles bearing a pure TRM and submitted to the Thellier–Coe protocol. Here, the laboratory field for the pTRM acquisitions was chosen identical to the field used to impart the original TRM. As illustrated in the inset of Figure 6a, the kinetic effects documented in Section 3.2 reveal themselves in the form of deflections from the straight line during the very first steps of the Thellier–Coe experiment where a steeper descent of the curve is observed. The deflections are observed over a reduced temperature interval of ∼0.01, corresponding to ∼6°C for magnetite, and are thus unlikely to be noticed in typical paleointensity experiments. Points in the Arai-Nagata diagram can be fitted by a straight line with a slope $b = 0.995$. Figure 6b presents another Thellier–Coe experiment when the laboratory field for the pTRM acquisitions was chosen twice lower. The points in this Arai-Nagata diagram can again be fitted by a straight line with a slope $b = 1.99$. The small deflections of b from the theoretical values of 1 and 2 are due to the previously mentioned kinetic effects. These two diagrams confirm that samples consisting of an ensemble of noninteracting SD particles bearing a pure TRM are well suited for API determinations. As a consequence, the choice of Thellier-style protocol (Thellier-Thellier, Thellier-Coe, or Thellier-Aitken) will only marginally affect the Arai-Nagata diagrams that yield the same API estimates.

Due to the very close similarity of TRM and TCRM intensities acquired by $T_{\rm c}$ increase (Section 3.1), the Arai-Nagata diagrams for such a TCRM are expected not to significantly differ from those presented in Figures 6a and 6b. An example of diagram for such TCRM acquired at reaction temperature $\theta_0 = 0.9$ is shown in Figure 6c. The API determined from this diagram leads to the slope $b = 1.03$ that only overestimates by 3% the applied field. This conclusion is fully consistent with the finding that a TCRM by $T_{\rm c}$ increase is very close to a pure TRM, with the nuance that small intensity excess of ca. 5% can occur at high energy parameter (Section 3.1, Figure 3). This result differs from the case considered by Fabian (2009) of an initial TRM later modified by partial grain dissolution or low-temperature oxidation, also producing a linear Arai-Nagata diagrams but significantly overestimating the paleointensity.

In contrast, Figure 6d shows the Arai-Nagata diagram for an ensemble of noninteracting SD particles bearing a TCRM acquired by grain-volume increase. This diagram reveals a conspicuous departure from the expected straight line, in the form of a convex curvature. The slope, close to one at low-temperature (red line in Figure 6d), quickly diminishes with θ_i increasing. We note that a similar behavior was reported for laboratory Thellier-type experiments on samples carrying a TCRM produced by single-phase oxidation of titanomagnetite grains at $T = 400$–500°C (Gribov et al., 2019), even if there is no obvious link between the two processes.

4.3. Peculiarities of IZZI Protocol

The IZZI protocol (Tauxe & Staudigel, 2004; Yu et al., 2004) is often claimed to be more efficient than other Thellier-type protocols to detect the presence of MD remanence carriers that would produce a zigzagging behavior of the points in the Arai-Nagata diagram in such a way that the IZ points (from successions of

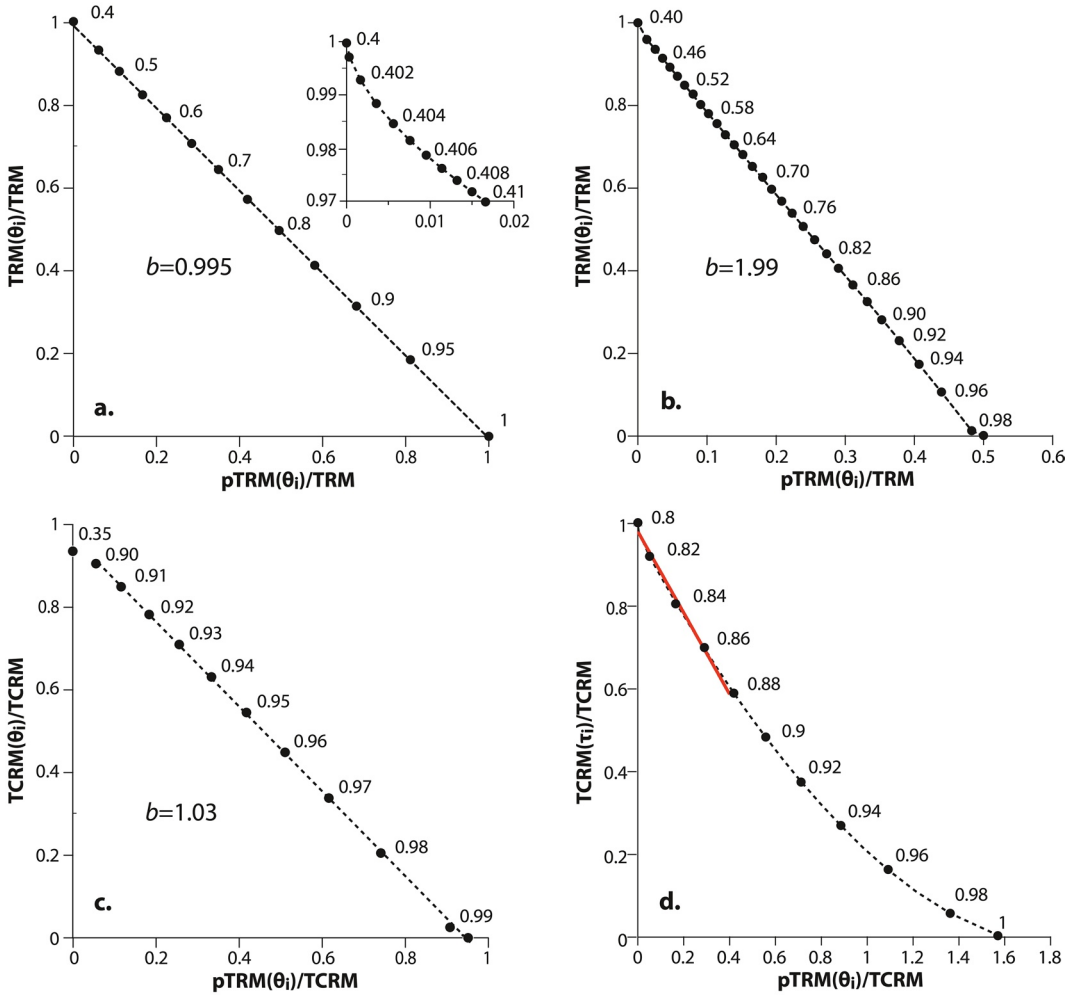

Figure 6. Modeling of Arai-Nagata diagrams for Thellier–Coe experiments. (a) TRM with a laboratory field identical to the ancient field. The inset enlarges the diagram for its initial part. The reduced temperature step $\Delta\theta = 0.002$ would for instance correspond to $\Delta T = 1.17$°C for magnetite. (b) TRM with a laboratory field twice bigger than the ancient field. (c) TCRM acquired by Curie temperature increase at reaction temperature $\theta_0 = 0.9$. (d) TCRM acquired by grain-volume increase at reaction temperature $\theta_0 = 0.8$. The quantity b corresponds to the best-fit slope.

in-field then zero-field heating–cooling cycles) lie systematically higher than the ZI points (from successions of zero-field then in-field heating–cooling cycles).

As illustrated in Figure 7a, the Arai-Nagata diagram, modeled for an ensemble of SD particles bearing a pure TRM, reveals small oscillations that can be explained by the kinetic effects reported in Section 3.2 according to which ZI and IZ heating–cooling cycles are not fully equivalent (Figures 4a and 4b). Indeed, the ratio (NRM loss)/(pTRM gain), measured after heating a grain to a temperature close to its blocking temperature, is significantly lower than 1 for the ZI cycle whereas it is very close to 1 for the IZ cycle. As illustrated in Figure 7b, we also reproduced the same oscillations from a direct experiment conducted on a thermally stable sample containing fine synthetic maghemite grains embedded in a kaolin matrix with relative volume concentration 0.5%. Based on hysteresis parameters (Mrs/Ms = 0.39, Bcr/Bc = 1.67) and the pTRM tail experiment shown in Figure 7c, we can claim that the grains are either of SD or small PSD size. According to these theoretical and experimental results, the zigzagging behavior of the IZZI protocol would not be a specificity of nonideal remanence carriers but is also found, in a modest proportion, for ideal SD carriers.

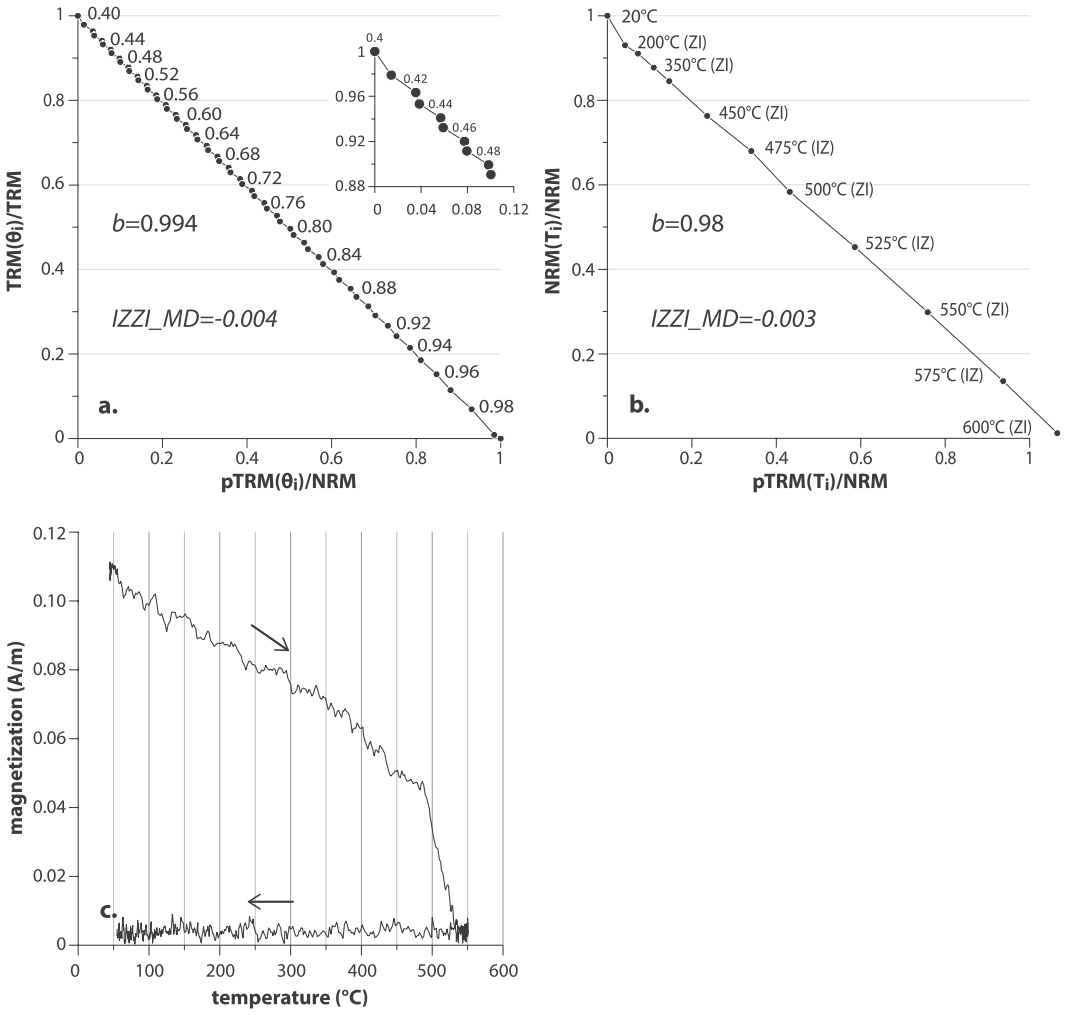

Figure 7. Particular case of the Thellier-IZZI protocol. (a) Modeled Arai-Nagata diagram. The reduced temperature step $\Delta\theta = 0.01$ would correspond to $\Delta T = 6.75$°C for maghemite. (b) Experimental Arai-Nagata diagram for a sample containing SD or small PSD grains (see Section 4.3). The quantities b and IZZI_MD denote the best-fit slope and the zigzagging quantifier (Shaar et al., 2011). (c) Continuous thermal demagnetization of a pTRM (550°C, 500°C) applied to the same sample as previously and revealing the absence of pTRM tail.

4.4. Effect of Cooling Rate on API Determinations

In first approximation, the cooling rate of natural rocks is governed by thermal diffusion and can be estimated by the relationship $\lambda \sim L^2/\chi$ where L is the smallest dimension of the magma reservoir/lava flow and $\chi \sim 10^{-6}$ m^2 s^{-1} is the typical thermal diffusivity of the magma/lava (e.g., Turcotte & Schubert, 2014). From this simple scaling rule, we can estimate that thin flows of 1-m thickness would cool down in approximately 10 days while thick flows of 10–30-m thickness would cool down in 3–30 years. In contrast, intrusions with L = 100–1,000 m would lead to $\lambda \sim 10^2$–10^4 years.

To model Arai-Nagata diagrams with different cooling rates, we used the same methodology as in Section 3.3, setting $q = q_0 + \ln(10)\, q_1$ for TRM acquisition and $q = q_0$ for pTRM acquisition and thermal demagnetization. We first considered the case of a ~100-m-thick intrusion with λ_{NRM} = 1,000 years. This value of λ_{NRM} relates to 650 years needed to cool down the rock over the entire blocking spectrum from $\theta_{b0} = 1$ to $\theta_{b0} = \theta_{low} = 0.5$. Figure 8a shows the modeled Arai-Nagata diagram and reveals a substantial overestimation of the paleointensity by 45%. As discussed in Section 3.3, a contrast in the efficiency of TRM acquisition exists between low and high θ_{b0}, which translates in Figure 8a into a small but noticeable curvature of the Arai-Nagata diagram, with a steeper slope at low θ_{b0}.

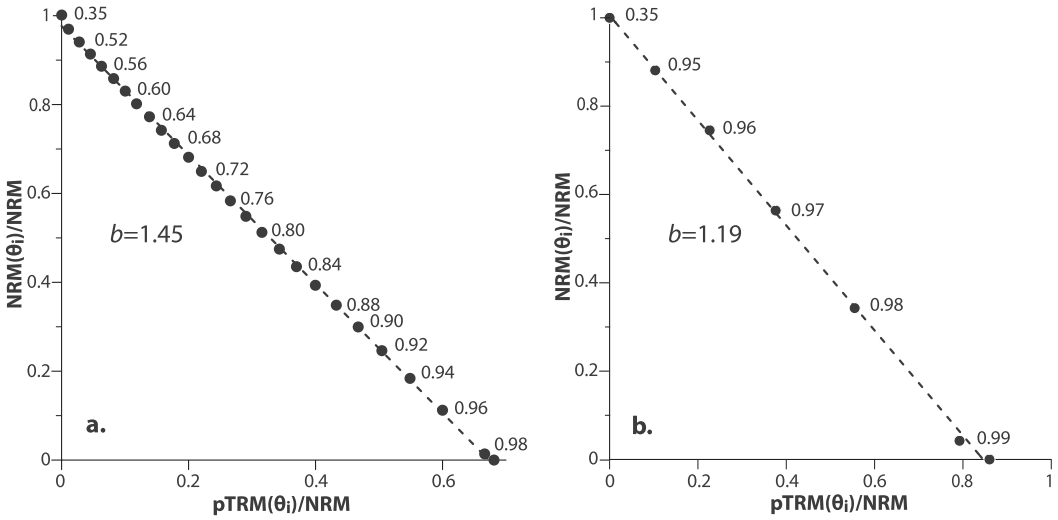

Figure 8. Effect of cooling rate on Arai-Nagata diagrams for Thellier-Coe experiments with a laboratory field identical to the ancient one. (a) TRM acquired for cooling time $\lambda_{NRM} = 1000$ years ($q = 42.6$ according to Equation 40). (b) TCRM acquired at reaction temperature $\theta_0 = 0.95$ for an annealing time of approximately one day. The quantity b stands for the best-fit slope.

We then considered the case of a NRM carried by a TCRM acquired by T_c increase while annealing a ~1-m-thick flow at $\theta_0 = 0.95$ (what would correspond to $T_0 \approx 520$°C for magnetite) during approximately one day. This leads to the parameters $\lambda_{NRM} = 20$ days and $q = 32.8$, where the annealing time was calculated from the relationship $\theta_c = \theta_0 + t/\lambda$ by taking $\theta_c = 1$. Figure 8b shows an overestimation of the paleointensity by 19%. Such a feature is in agreement with the experimental results by Yamamoto et al. (2003) and Yamamoto (2006) that documented overestimated paleointensisties by 10%–50% for the historical 1960 Kilauea lava flow, interpreted as the result of a TCRM acquired by grain-volume growth. The presence of titanomagnetite grains with well-developed ilmenite lamellae together with exsolved titanohematite grains could also point to a TCRM acquired by T_c increase during the exsolution process below T_c, that is, in similar conditions to the experimental case investigated by Shcherbakov et al. (2019).

4.5. Effect of SV on API Determinations

We now consider the case when the cooling time of igneous rocks is slow enough to coincide with the typical time scales of geomagnetic SV, which are known to be on the order of a few millennia for the dipole component and on the order of a few centuries for the dominant multipolar components (e.g., Hongre et al., 1998; Hulot & Le Mouël, 1994; Lhuillier et al., 2011). In this case, every sub-ensemble of grains with a given blocking temperature witnesses a different field. In this paper, we neglect the effect of the directional fluctuations on the shape of the Arai-Nagata diagrams, assuming that the directional fluctuations produce equivalent intensity changes (e.g., a 6% intensity change for a 20° directional deflection) that are small enough compared to the changes of the geomagnetic field strength. To assess the secular-variation effect in the framework of this approximation, we modeled the field variations $h(t)$ by a Giant Gaussian Process (e.g., Constable & Parker, 1988; Khokhlov & Hulot, 2013) and used the algorithm proposed by Khokhlov and Shcherbakov (2015) to generate intensity data. These data were first normalized to the average over the chosen time interval so that $h(t)$ becomes dimensionless. Next, the function $h(t)$ was converted to $h(\theta)$ and substituted in Equations 15 and 17. Arai-Nagata diagrams were modeled following the same methodology as in the previous sections. We additionally computed the derivative $h^*(\theta) = \mathrm{d(NRM)/d(pTRM)}$ that represents the local value of the paleointensity in the Arai-Nagata diagram.

Figures 9a and 9b present examples of Arai-Nagata diagrams for TRMs acquired at cooling time $\lambda_{NRM} = 1000$ years (i.e., for $q = 42.6$ according to Equation 40) in the presence of a time-variable external field $h(\theta)$ with $\theta = 1 - t/\lambda$ ($\lambda \geq 0.5$). We first note that the slopes averaged over the whole temperature spectrum ($b = 1.39$ for Figure 9a, $b = 1.4$ for Figure 9b) lead to an overestimation of the recovered paleointensity

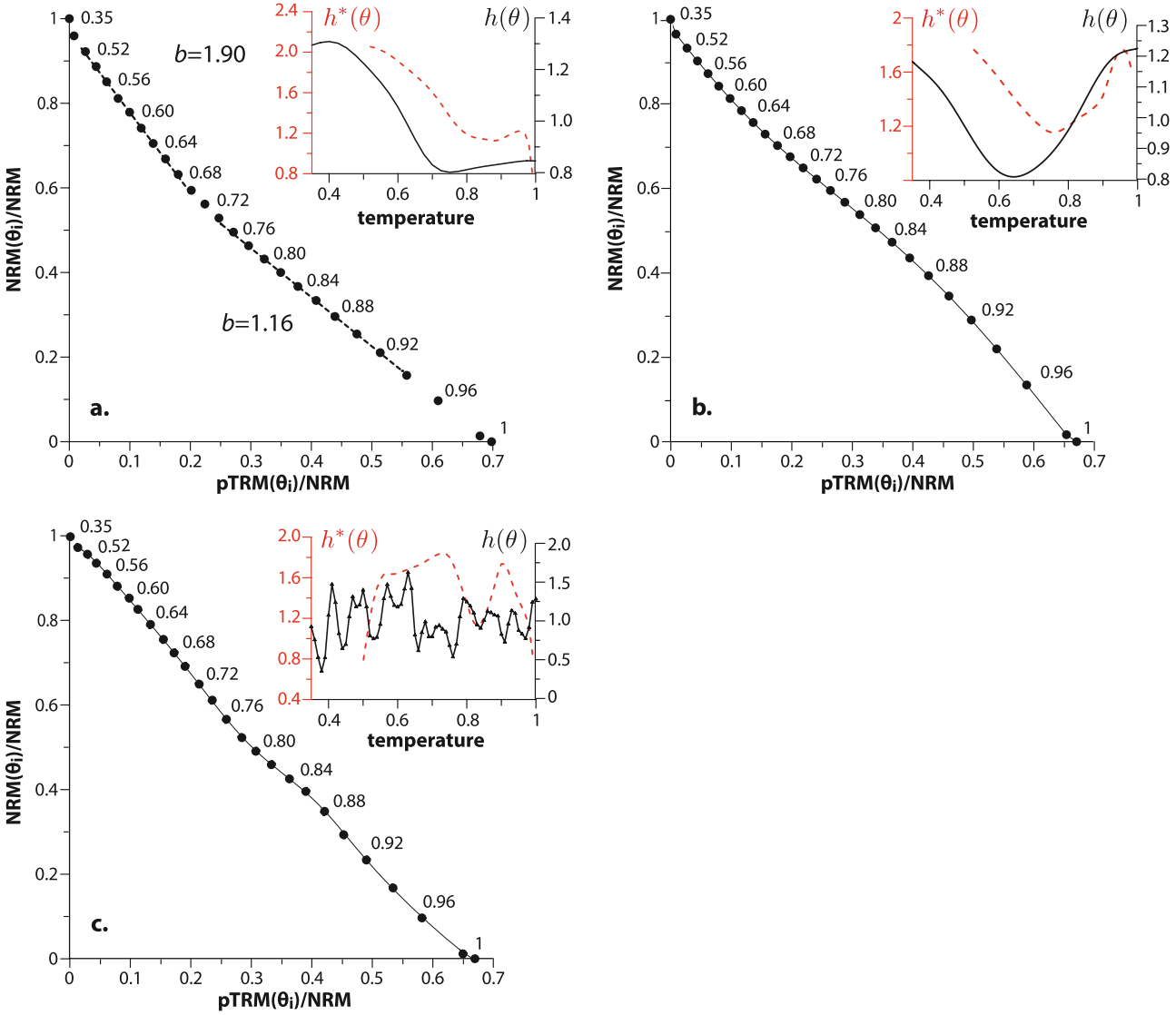

Figure 9. Effect of secular variation on Arai-Nagata diagrams for Thellier–Coe experiments. (a and b) TRM acquired for cooling time λ_{NRM} = 1,000 years (i.e., q = 42.6). (c) TRM acquired for cooling time λ_{NRM} = 10,000 years (i.e., q = 44.9). The variations of the normalized external field $h(\theta = 1 - t / \lambda | \lambda \geq 0.5)$ during the TRM acquisition (solid line, right axis in the insets) were predicted by the statistical model by Khokhlov and Shcherbakov (2015). The local value of the paleointensity in the Arai-Nagata diagrams is represented by the derivative $h^*(\theta)$ = d(NRM)/d(pTRM) (dashed line, left axis in the insets).

by ca. 40%. Such a value is in overall agreement with the case investigated in Section 4.4 (Figure 8) for a TRM acquired in the presence of a constant external field at the same cooling rate and is thus the signature of the cooling-rate effect. However, Figures 9a and 9b indicate that the shape of the Arai-Nagata diagrams schematically reflects the variations of the external field $h(\theta)$ during TRM acquisition. Figure 9a shows a two-slope diagram with (i) a moderate slope b = 1.16 for $\theta > 0.75$ corresponding to the sample's cooling in a nearly constant field $h \approx 0.85$ and (ii) a steeper slope b = 1.90 for $\theta < 0.75$ corresponding to the sample's cooling in a field gradually increasing from $h \approx 0.8$ to 1.2. Figure 9b considers the case of a V-shaped variation of the external field leading to a minimum of the slope at mid-temperature in the Arai-Nagata diagram. A more thorough analysis of the Arai-Nagata diagrams is made by comparing the derivative $h^*(\theta)$ of the curve with the external field $h(\theta)$ during TRM acquisition. The insets of Figures 9a and 9b reveal that the curves $h(\theta)$ and $h^*(\theta)$ display the same morphology but with a shift $\Delta\theta \approx 0.1$ toward higher temperatures for $h^*(\theta)$. In other words, it means that the paleointensity recovered at a given temperature corresponds to an external field seen at a lower temperature. This can be seen as a direct consequence of the cooling-rate effect detailed

in Section 3.3 (Figure 5a) according to which the blocking temperature of the TRM in laboratory conditions (i.e., for $q_1 = 0$) is higher than the blocking temperature of the NRM in natural conditions (i.e., for $q_1 > 0$).

Figure 9c finally deals with the case of an NRM acquired at cooling time $\lambda_{NRM} = 10{,}000$ years (i.e., for $q = 44.9$ according to Equation 40) such that the cooling time largely exceeds the typical SV time scales of Earth's magnetic field, with the intention of mimicking the effect of averaging SV. The Arai-Nagata diagram yields an average slope $b = 1.53$, the overestimated value of which can be explained once more by the cooling rate effect. In contrast to Figures 9a and 9b, the external field $h(\theta)$ experience multiple extrema but the points in the Arai-Nagata diagram only show small fluctuations around the linear trend. In this configuration, the variations of $h^*(\theta)$ are again shifted toward higher temperatures as a result of the cooling-rate effect but are also very smoothed with respect to the variations of $h(\theta)$. In summary, these observations indicate that Thellier-type API determinations on slowly cooled assemblies of noninteracting SD grains are trustworthy provided that SV is sufficiently averaged out and that a cooling-rate correction is applied.

More generally, one can wonder what would be the best approach to obtain API estimates that are representative of the geodynamo's state. A first possibility is to rely on rapidly cooled lava flows that yield quasi-instantaneous records of Earth's magnetic field. The best examples are the basaltic glasses (e.g., Cromwell et al., 2015, 2018) for which the natural and laboratory cooling rates are thought to be of the same order of magnitude (e.g., Gottsmann et al., 2004). The drawback of this method is that determinations from multiple cooling units are necessary to average out SV. A second possibility is to rely on slowly cooled intrusions, the cooling time of which largely exceeds the typical SV time scales. Such an approach was for instance recently employed by Bono et al. (2019) in their study of the Ediacaran Sept-Îles intrusive suite. Assuming a cooling time of ∼75 Kyr over the blocking temperature interval, a cooling-rate correction factor of ∼1.5 was then applied to their raw results. The drawback of this method is that an estimate of the NRM's cooling rate is mandatory and that the cooling-rate correction will be difficult in the case of nonideal remanence carriers. Between these two end-member cases, caution must be exercised. We showed that, when the NRM's cooling time coincides with the typical SV time scales of Earth's magnetic field, the shape of the Arai-Nagata can be strongly deformed and make their correct interpretation impossible.

5. Concluding Remarks

Exact analytical solutions of the kinetic equations for the acquisition and thermal demagnetization of TRM and TCRMs acquired by grain-volume growth or Curie temperature increase were derived in SD grains and used to model the outcome of API determinations for different variants of Thellier's protocol.

1. For the fictitious and nonrealistic case of assemblies of identical SD grains, Thellier's law of independence is often violated as a consequence of the noninstantaneousness of the blocking process. The Thellier-Thellier and Thellier-Aitken protocols are in this case the only acceptable options whereas the Thellier-Coe protocol underestimates the paleofield by several tens of percents.
2. For the more realistic case of assemblies of coercivity-variable SD grains, the previously mentioned effects largely compensate each other. All Thellier-type protocols yield reliable paleofields for TRMs and TCRMs acquired by T_c increase, with the nuance that (i) small deflections of the slopes are observed for the Thellier-Coe protocol for the very initial points in the Arai-Nagata diagram and (ii) small zigzags around the linear trend are identified in the Arai-Nagata diagram for the Thellier-IZZI protocol. In contrast, TCRMs acquired by grain-volume growth yield convex Arai-Nagata diagrams that are challenging to interpret.
3. The most conspicuous kinetic effect is the influence of cooling rate, with a ∼5% increase in the remanence intensity corresponding to a tenfold increase in the cooling time. If the cooling time coincides with the geomagnetic SV time scales, the time-dependent remanence acquisition may lead to ambiguous Arai-Nagata diagrams with multiple slopes. If the cooling time conversely average out SV, the API determinations are reliable provided that a cooling-rate correction is possible.
4. The corollary of these kinetic effects is that several causes (TCRMs acquired by volume-grain growth, insufficient averaging of geomagnetic SV for slowly cooled units) can yield convex Arai-Nagata diagrams, the shape of which is difficult to distinguish from the deformations produced by nonideal MD remanence carriers (e.g., Calvo et al., 2002; Kosterov & Prévot, 1998; Levi, 1977; Xu & Dunlop, 2004).

As a last remark, we would like to mention that the analytical solutions presented in this paper were derived for assemblies of noninteracting SD grains with shape anisotropy. We show in Appendix B that the assumption of shape anisotropy probably has little influence on the kinetic processes. However, generalizing the results to assemblies of PSD grains, even for those of small size containing few energy minima (e.g., Fabian & Shcherbakov, 2018), would need a substantial amount of work. Another open question is the effect of interactions on the shape of Arai-Nagata diagrams (e.g., Coe, 1974; Shcherbakov, Sycheva, et al., 1996).

Appendix A: Generalization for Exponential Cooling-Time Dependency

We considered in Section 2.2 a linear dependency $\theta(t) = \theta_0 + t/\lambda$ of temperature on time. It is unfortunately impossible to integrate Equation 8 for any time dependency. However, an exponential dependency $\theta(t) = \theta_0 \exp(-t/\lambda)$ can be easily handled, in which case Equation 8 can be transformed into

$$\frac{\mathrm{d}y}{\mathrm{d}\theta} = -2\, f_0\, \lambda\, \theta \exp\left(-\frac{\mu_0\, N_\mathrm{d}\, M_\mathrm{S}^2\, V}{2\, k_\mathrm{B}\, T}\right)\left(y - \frac{\mathbf{m}\cdot\mathbf{B}}{k_\mathrm{B}\, T}\right). \tag{A1}$$

It entails that Equation 9 can still be used with the new coefficient

$$A(\theta) = \frac{1}{\theta}\exp\left(q + g - \frac{g}{\theta}\right), \tag{A2}$$

which leads to the new expression

$$f(\theta) = \int A(x)\,\mathrm{d}x = \exp(q+g)\,\Gamma(0, g/\theta) \tag{A3}$$

that is even simpler than Equation 16 for a linear dependency of temperature on time. Nevertheless, it appears that the TRM intensities for an assembly of noninteracting SD grains (Equation 46) yield indistinguishable results when calculated from Equation 16 for a linear dependency and from Equation A3 for an exponential dependency. For the sake of simplicity, we thus considered a linear dependency in this paper.

Appendix B: Generalization for NonShape Anisotropy

Let us abandon the assumption of uniaxial shape anisotropy described by Equation 5 and consider the more general relationship

$$E_\mathrm{b} = \frac{mB_\mathrm{c}}{k_\mathrm{B}\, T} = N M_{\mathrm{S}0}^2 j_s^n \tag{B1}$$

where N and n are the energy parameters. Equation 10 can thus be rewritten as

$$A(\theta) = \exp\left[q + g\frac{(1-\theta)^{n/2}}{\theta}\right]. \tag{B2}$$

Unfortunately, for $n \neq 2$, the integral $f(\theta) = \int A(\theta)\,\mathrm{d}\theta$ has no analytical solution. To approximate this integral, we thus used the approach proposed by Dodson and McClelland-Brown (1980) whereby Boltzmann's factor $\exp(q - E_\mathrm{b})$ is replaced by

$$\exp\left[q - \left(\frac{m\, B_\mathrm{c}}{k_\mathrm{B}\, T}\right)_{T=T_1} - \frac{\mathrm{d}}{\mathrm{d}T}\left(\frac{mB_\mathrm{c}}{k_\mathrm{B}\, T}\right)_{T=T_1}(T - T_1).\right] \tag{B3}$$

Here, T_1 is a temperature chosen to eliminate the constant term of the decomposition, that is, by the condition

$$q = \left(\frac{mH_c}{kT}\right)_{T=T_1} \quad \text{or} \quad q = g(1-\theta_1)^{n/2} / \theta_1. \tag{B4}$$

Equation B2 can thus be simplified into

$$A(\theta) = \exp\left[a(\theta - \theta_1)\right] \quad | \quad a = \frac{g(1-\theta_1)^{\frac{n-2}{2}}(2+(n-2)\theta_1)}{2\theta_1^2} \tag{B5}$$

leading to

$$f(\theta) = \frac{1}{a}\exp[a(\theta - \theta_1)]. \tag{B6}$$

For $n = 2$ (shape anisotropy) $a = g / \theta_1^2$ and $\theta_1 = g/(q + g)$. For $n = 4$ $a = 1 / \theta_1^2 - 1$ and $\theta_1 = \left[2g + q - \sqrt{q(4g+q)}\right] / (2g)$. The solutions $y(\theta)$ for these two cases are shown in Figure B1a. As expected, the blocking temperature for $n = 4$ is considerably lower than for $n = 2$. In other words, blocking temperatures shift down with n increasing due to the decrease of the potential barrier E_b.

The validity of this approximation can be tested for $n = 2$ by comparing the solutions with the exact formulas from Section 2. As illustrated in Figures B1b and B1c, the similarity between the exact and approximated solutions is quite satisfactory. It gives hope that calculations carried out by the approximate algorithm can provide adequate solutions to other values of n, though this statement might not be conclusive until more evidence is obtained.

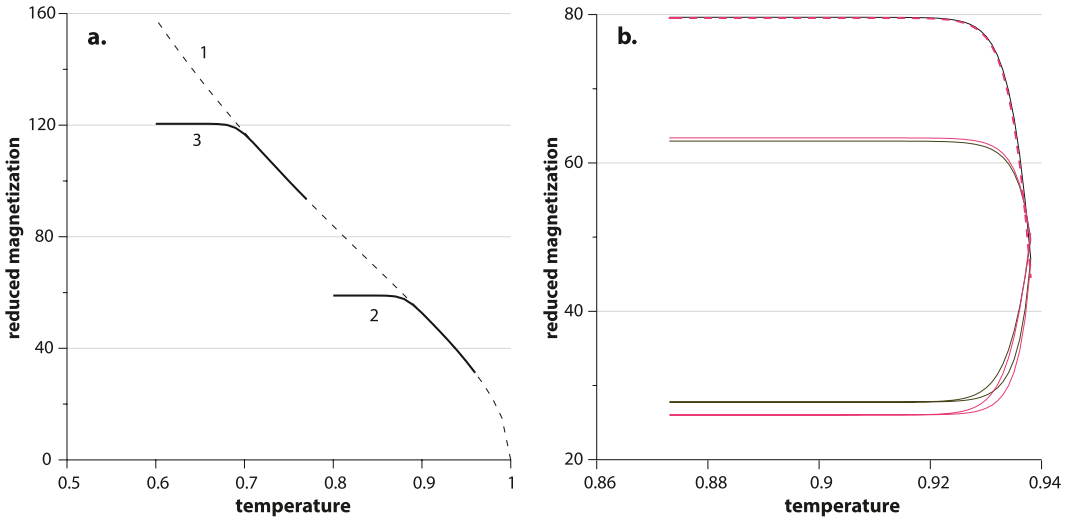

Figure B1. Generalization for nonshape anisotropy. (a) Example of TRM acquisition for parameters $g = 150$ and $q = 25$. Curve 1 shows the reference curve $y(\theta) = \sqrt{1-\theta} / \theta$ for an ensemble of SP grains at equilibrium. Curves 2 and 3 show the reduced magnetization $y(\theta)$ for energy parameter $n = 2$ and $n = 4$, respectively. (b) Zero-field followed by in-field heating–cooling cycles to an intermediate temperature $\theta_i = 0.938$ for parameters $g = 150$ and $q = 25$. The black curves show the exact solutions whereas the red curves show the approximated solutions.

Data Availability Statement

None.

Acknowledgments
All the information necessary to reproduce the conclusions of this theoretical paper are provided in Section 2. The reported study was funded by Russian Science Foundation grant 19-47-04110 (VS), DFG grant LH55/5-1 (FL), and RFBR, project number 20-05-00,215 (NKS). We thank Mark Dekkers and Bjarne Almqvist for editorial handling, as well as the two reviewers Bruce Moskowitz and Adrian Muxworthy for their constructive comments.
Open access funding enabled and organized by Projekt DEAL.

References

Aitken, M. J., Allsop, A. L., Bussell, G. D., & Winter, M. B. (1988). Determination of the intensity of the Earth's magnetic field during archeological times: Reliability of the Thellier Technique. *Reviews of Geophysics*, *26*(1), 3–12. https://doi.org/10.1029/RG026i001p00003

Bean, C. P., & Livingston, J. D. (1959). Superparamagnetism. *Journal of Applied Physics*, *30*(4), S120–S129. https://doi.org/10.1063/1.2185850

Berndt, T. A., Chang, L., Paterson, G. A., & Cao, C. (2020). Experimental test of the cooling rate effect on blocking temperatures in stepwise thermal demagnetization. *Geophysical Journal International*, *224*(2), 1116–1126. https://doi.org/10.1093/gji/ggaa514

Berndt, T., Paterson, G. A., Cao, C., & Muxworthy, A. R. (2017). Experimental test of the heating and cooling rate effect on blocking temperatures. *Geophysical Journal International*, *210*(1), 255–269. https://doi.org/10.1093/gji/ggx153

Biggin, A. J., Badejo, S., Hodgson, E., Muxworthy, A. R., Shaw, J., & Dekkers, M. J. (2013). The effect of cooling rate on the intensity of thermoremanent magnetization (TRM) acquired by assemblages of pseudo-single domain, multidomain and interacting single-domain grains. *Geophysical Journal International*, *193*(3), 1239–1249. https://doi.org/10.1093/gji/ggt078

Biggin, A. J., Piispa, E. J., Pesonen, L. J., Holme, R., Paterson, G. A., Veikkolainen, T., & Tauxe, L. (2015). Paleomagnetic field intensity variations suggest Mesoproterozoic inner-core nucleation. *Nature*, *526*(7572), 245–248. https://doi.org/10.1038/nature15523

Bono, R. K., Tarduno, J. A., Nimmo, F., & Cottrell, R. D. (2019). Young inner core inferred from Ediacaran ultra-low geomagnetic field intensity. *Nature Geoscience*, *12*(2), 143–147. https://doi.org/10.1038/s41561-018-0288-0

Bowles, J. A., & Jackson, M. J. (2016). Effects of titanomagnetite reordering processes on thermal demagnetization and paleointensity experiments. *Geochemistry, Geophysics, Geosystems*, *17*(12), 4848–4858. https://doi.org/10.1002/2016GC006607

Bowles, J. A., Jackson, M. J., Berquó, T. S., Sølheid, P. A., & Gee, J. S. (2013). Inferred time- and temperature-dependent cation ordering in natural titanomagnetites. *Nature Communications*, *4*, 1916–1919. https://doi.org/10.1038/ncomms2938

Brown, W. F. (1962). Magnetostatic principles in ferromagnetism (Vol. 1). North-Holland Publishing Company.

Calvo, M., Prévot, M., Perrin, M., & Riisager, J. (2002). Investigating the reasons for the failure of palaeointensity experiments: A study on historical lava flows from Mt. Etna (Italy). *Geophysical Journal International*, *149*(1), 44–63. https://doi.org/10.1046/j.1365-246X.2002.01619.x

Coe, R. S. (1967). The determination of paleo-intensities of the earth's magnetic field with emphasis on mechanisms which could cause non-ideal behavior in Thellier's method. *Journal of Geomagnetism Geoelectricity*, *19*(3), 157–179. https://doi.org/10.5636/jgg.19.157

Coe, R. S. (1974). The effect of magnetic interactions on paleointensity determinations by the Thelliers' method. *Journal of Geomagnetism Geoelectricity*, *26*(3), 311–317. https://doi.org/10.5636/jgg.26.311

Constable, C. G., & Parker, R. L. (1988). Statistics of the geomagnetic secular variation for the past 5 m.y. *Journal of Geophysical Research*, *93*(B10), 11569–11581. https://doi.org/10.1029/JB093iB10p11569

Cromwell, G., Tauxe, L., Staudigel, H., & Ron, H. (2015). Paleointensity estimates from historic and modern Hawaiian lava flows using glassy basalt as a primary source material. *Physics of the Earth and Planetary Interiors*, *241*(C), 44–56. https://doi.org/10.1016/j.pepi.2014.12.007

Cromwell, G., Trusdell, F., Tauxe, L., Staudigel, H., & Ron, H. (2018). Holocene paleointensity of the Island of Hawai `i from glassy volcanics. *Geochemistry, Geophysics, Geosystems*, *19*(9), 3224–3245. https://doi.org/10.1002/2017GC006927

Dodson, M. H., & McClelland-Brown, E. (1980). Magnetic blocking temperatures of single-domain grains during slow cooling. *Journal of Geophysical Research*, *85*(B5), 2625–2637. https://doi.org/10.1029/JB085iB05p02625

Draeger, U., Prévot, M., Poidras, T., & Riisager, J. (2006). Single-domain chemical, thermochemical and thermal remanences in a basaltic rock. *Geophysical Journal International*, *166*(1), 12–32. https://doi.org/10.1111/j.1365-246X.2006.02862.x

Dunlop, D. J. (2011). Physical basis of the Thellier-Thellier and related paleointensity methods. *Physics of the Earth and Planetary Interiors*, *187*(3–4), 118–138. https://doi.org/10.1016/j.pepi.2011.03.006

Dunlop, D. J., & Özdemir, Ö. (1997). *Rock magnetism: Fundamentals and frontiers*. Cambridge University Press. https://doi.org/10.1017/CBO9780511612794

Egli, R., & Lowrie, W. (2002). Anhysteretic remanent magnetization of fine magnetic particles. *Journal of Geophysical Research*, *107*(B10), 2–1. https://doi.org/10.1029/2001JB000671

Fabian, K. (2009). Thermochemical remanence acquisition in single-domain particle ensembles: A case for possible overestimation of the geomagnetic paleointensity. *Geochemistry, Geophysics, Geosystems*, *10*(6), 1–10. https://doi.org/10.1029/2009GC002420

Fabian, K., & Shcherbakov, V. P. (2018). Energy barriers in three-dimensional micromagnetic models and the physics of thermoviscous magnetization. *Geophysical Journal International*, *215*(1), 314–324. https://doi.org/10.1093/gji/ggy285

Ferk, A., Leonhardt, R., Hess, K. U., Koch, S., Egli, R., Krása, D., & Dingwell, D. B. (2014). Influence of cooling rate on thermoremanence of magnetite grains: Identifying the role of different magnetic domain states. *Journal of Geophysical Research: Solid Earth*, *119*(3), 1599–1606. https://doi.org/10.1002/2013JB010845

Gottsmann, J., Harris, A. J. L., & Dingwell, D. B. (2004). Thermal history of Hawaiian pāhoehoe lava crusts at the glass transition: Implications for flow rheology and emplacement. *Earth and Planetary Science Letters*, *228*(3–4), 343–353. https://doi.org/10.1016/j.epsl.2004.09.038

Gribov, S. K., Shcherbakov, V. P., & Aphinogenova, N. A. (2019). Magnetic properties of artificial CRM created on titanomagnetite-bearing Oceanic Basalts. In D. Nurgaliev, V. Shcherbakov, A. Kosterov, & S. Spassov (Eds.), *Recent advances in rock magnetism, environmental magnetism and paleomagnetism* (pp. 173–194). Springer International Publishing. https://doi.org/10.1007/978-3-319-90437-5_14

Halgedahl, S. L., Day, R., & Fuller, M. (1980). The effect of cooling rate on the intensity of weak-field TRM in single-domain magnetite. *Journal of Geophysical Research*, *85*(B7), 3690–3698. https://doi.org/10.1029/JB085iB07p03690

Hongre, L., Hulot, G., & Khokhlov, A. (1998). An analysis of the geomagnetic field over the past 2000 years. *Physics of the Earth and Planetary Interiors*, *106*(3–4), 311–335. https://doi.org/10.1016/S0031-9201(97)00115-5

Hulot, G., & Le Mouël, J.-L. (1994). A statistical approach to the Earth's main magnetic field. *Physics of the Earth and Planetary Interiors*, *82*(3–4), 167–183. https://doi.org/10.1016/0031-9201(94)90070-1

Ingham, E., Heslop, D., Roberts, A. P., Hawkins, R., & Sambridge, M. (2014). Is there a link between geomagnetic reversal frequency and paleointensity? A Bayesian approach. *Journal of Geophysical Research: Solid Earth*, *119*(7), 5290–5304. https://doi.org/10.1002/2014JB010947

Jackson, M., & Bowles, J. (2018). Malleable Curie temperatures of natural titanomagnetites: Occurrences, modes, and mechanisms. *Journal of Geophysical Research: Solid Earth*, *123*(1), 921–940. https://doi.org/10.1002/2017JB015193

Khokhlov, A., & Hulot, G. (2013). Probability uniformization and application to statistical paleomagnetic field models and directional data. *Geophysical Journal International*, *193*(1), 110–121. https://doi.org/10.1093/gji/ggs118

Khokhlov, A., & Shcherbakov, V. (2015). Palaeointensity and Brunhes paleomagnetic field models. *Geophysical Journal International*, *202*(2), 1419–1428. https://doi.org/10.1093/gji/ggv236

Kono, M. (1974). Intensities of the Earth's magnetic field about 60 m.y. ago determined from the Deccan Trap Basalts, India. *Journal of Geophysical Research*, *79*(8), 1135–1141. https://doi.org/10.1029/JB079i008p01135

Kosterov, A. A., & Prévot, M. (1998). Possible mechanisms causing failure of Thellier palaeointensity experiments in some Basalts. *Geophysical Journal International*, *134*(2), 554–572. https://doi.org/10.1046/j.1365-246x.1998.00581.x

Kulakov, E. V., Sprain, C. J., Doubrovine, P. V., Smirnov, A. V., Paterson, G. A., Hawkins, L., et al. (2019). Analysis of an updated paleointensity database (QPI-PINT) for 65-200 Ma: Implications for the long-term history of dipole moment through the Mesozoic. *Journal of Geophysical Research: Solid Earth*, *124*(10), 9999–10022. https://doi.org/10.1029/2018JB017287

Levi, S. (1977). The effect of magnetite particle size on paleointensity determinations of the geomagnetic field. *Physics of the Earth and Planetary Interiors*, *13*(4), 245–259. https://doi.org/10.1016/0031-9201(77)90107-8

Lhuillier, F., Fournier, A., Hulot, G., & Aubert, J. (2011). The geomagnetic secular-variation timescale in observations and numerical dynamo models. *Geophysical Research Letters*, *38*(9). https://doi.org/10.1029/2011GL047356

Nagata, T., Arai, Y., & Momose, K. (1963). Secular variation of the geomagnetic total force during the last 5000 years. *Journal of Geophysical Research*, *68*(18), 5277–5281. https://doi.org/10.1029/j.2156-2202.1963.tb00005.x

Néel, L. (1949). Théorie du traînage magnétique des ferromagnétiques en grains fins avec applications aux terres cuites. *Annals of Geophysics*, *5*, 99–136.

Néel, L. (1955). Some theoretical aspects of rock-magnetism. *Advances in Physics*, *4*(14), 191–243. https://doi.org/10.1080/00018735500101204

Selkin, P. A., & Tauxe, L. (2000). Long-term variations in palaeointensity. *Philosophical Transactions of the Royal Society of London,Series A: Mathematical, Physical and Engineering Sciences*, *358*(1768), 1065–1088. https://doi.org/10.1098/rsta.2000.0574

Shaar, R., Ron, H., Tauxe, L., Kessel, R., & Agnon, A. (2011). Paleomagnetic field intensity derived from non-SD: Testing the Thellier IZZI technique on md slag and a new bootstrap procedure. *Earth and Planetary Science Letters*, *310*(3–4), 213–224. https://doi.org/10.1016/j.epsl.2011.08.024

Shcherbakov, V. P., & Fabian, K. (2005). On the determination of magnetic grain-size distributions of superparamagnetic particle ensembles using the frequency dependence of susceptibility at different temperatures. *Geophysical Journal International*, *162*(3), 736–746. https://doi.org/10.1111/j.1365-246X.2005.02603.x

Shcherbakov, V. P., & Sycheva, N. K. (2013). On the intensity of the geomagnetic field in the geological past. *Izvestiya, Physics of the Solid Earth*, *49*(5), 699–717. https://doi.org/10.1134/S1069351313040095

Shcherbakov, V. P., Gribov, S. K., Lhuillier, F., Aphinogenova, N. A., & Tsel'movich, V. A. (2019). On the reliability of absolute palaeointensity determinations on basaltic rocks bearing a thermochemical remanence. *Journal of Geophysical Research: Solid Earth*, *124*(3), 7616–7632. https://doi.org/10.1029/2019JB017873

Shcherbakov, V. P., McClelland, E., & Shcherbakova, V. V. (1993). A model of multidomain thermoremanent magnetization incorporating temperature-variable domain structure. *Journal of Geophysical Research*, *98*(B4), 6201–6216. https://doi.org/10.1029/92JB02572

Shcherbakov, V. P., Sycheva, N. K., & Lamash, B. E. (1996). Monte Carlo modeling of TRM and CRM acquisition and comparison of their properties in an ensemble of interacting SD grains. *Geophysical Research Letters*, *23*(20), 2827–2830. https://doi.org/10.1029/96GL01999

Smirnov, A. V., & Tarduno, J. A. (2005). Thermochemical remanent magnetization in Precambrian rocks: Are we sure the geomagnetic field was weak? *Journal of Geophysical Research*, *110*(B6), 10–12. https://doi.org/10.1029/2004JB003445

Smirnov, A. V., Tarduno, J. A., Kulakov, E. V., McEnroe, S. A., & Bono, R. K. (2016). Palaeointensity, core thermal conductivity and the unknown age of the inner core. *Geophysical Journal International*, *205*(2), 1190–1195. https://doi.org/10.1093/gji/ggw080

Stacey, F. D., & Banerjee, S. K. (1974). *The physical principles of rock magnetism*. Elsevier.

Tarduno, J. A., Cottrell, R. D., Davis, W. J., Nimmo, F., & Bono, R. K. (2015). A Hadean to Paleoarchean geodynamo recorded by single zircon crystals. *Science*, *349*(6247), 521–524. https://doi.org/10.1126/science.aaa9114

Tauxe, L., & Staudigel, H. (2004). Strength of the geomagnetic field in the Cretaceous Normal Superchron: New data from submarine basaltic glass of the Troodos Ophiolite. *Geochemistry, Geophysics, Geosystems*, *5*(2). https://doi.org/10.1029/2003GC000635

Tauxe, L., & Yamazaki, T. (2015). Paleointensities. In M. Kono, & G. Schubert, (Eds.), *Geomagnetism* (pp. 461–509). Elsevier B.V. https://doi.org/10.1016/B978-0-444-53802-4.00107-X

Thellier, E., & Thellier, O. (1959). Sur l'intensité du champ magnétique terrestre dans le passé historique et géologique. *Annales de Geophysique*, *15*(3), 285–376.

Turcotte, D., & Schubert, G. (2014). *Geodynamics* (3rd ed.). Cambridge University Press. https://doi.org/10.1017/cbo9780511843877

Valet, J.-P. (2003). Time variations in geomagnetic intensity. *Reviews of Geophysics*, *41*(1), 1004. https://doi.org/10.1029/2001RG000104

Walton, D. (1980). Time-temperature relations in the magnetization of assemblies of single domain grains. *Nature*, *286*(5770), 245–247. https://doi.org/10.1038/286245a0

Xu, S., & Dunlop, D. J. (2004). Thellier paleointensity theory and experiments for multidomain grains. *Journal of Geophysical Research*, *109*(B7), 279. https://doi.org/10.1029/2004JB003024

Yamamoto, Y. (2006). Possible TCRM acquisition of the Kilauea 1960 lava, Hawaii: Failure of the Thellier paleointensity determination inferred from equilibrium temperature of the Fe–Ti oxide. *Earth, Planets and Space*, *58*(8), 1033–1044. https://doi.org/10.1186/BF03352608

Yamamoto, Y., Tsunakawa, H., & Shibuya, H. (2003). Palaeointensity study of the Hawaiian 1960 lava: Implications for possible causes of erroneously high intensities. *Geophysical Journal International*, *153*(1), 263–276. https://doi.org/10.1046/j.1365-246X.2003.01909.x

York, D. (1978). Magnetic blocking temperature. *Earth and Planetary Science Letters*, *39*(1), 94–97. https://doi.org/10.1016/0012-821X(78)90145-0

Yu, Y. (2011). Importance of cooling rate dependence of thermoremanence in paleointensity determination. *Journal of Geophysical Research*, *116*(B9), 3. https://doi.org/10.1029/2011JB008388

Yu, Y., Tauxe, L., & Genevey, A. (2004). Toward an optimal geomagnetic field intensity determination technique. *Geochemistry, Geophysics, Geosystems*, *5*(2). https://doi.org/10.1029/2003GC000630